

***J*-integral Approach to Estimation of Tensile Strain Capacity  
in Strain-based Design**

M. Reza Hirmand, William R. Tyson, Su Xu, Timothy S. Weeks

**Report No. CMAT-2021-WF 63142104**

July 2021

**CMAT**

## **DISCLAIMER**

Natural Resources Canada makes no representations or warranties respecting the contents of this report, either expressed or implied, arising by law or otherwise, including but not limited to implied warranties or conditions of merchantability or fitness for a particular purpose.

CanmetMATERIALS

REPORT CMAT-2021-WF 63142104

*J*-INTEGRAL APPROACH TO ESTIMATION OF TENSILE STRAIN CAPACITY IN STRAIN-BASED DESIGN

by

M. Reza Hirmand<sup>1</sup>, William R. Tyson<sup>1</sup>, Su Xu<sup>1</sup>, Timothy S. Weeks<sup>2</sup>

<sup>1</sup>CanmetMATERIALS, Natural Resources Canada, Hamilton, ON, Canada

<sup>2</sup>National Institute of Standards and Technology, Boulder, CO, USA

**EXECUTIVE SUMMARY**

This report revisits previous numerical predictions and experimental measurements of tensile strain capacity (TSC) in curved wide plate (CWP) specimens. The tests [1,2] were performed under a U.S. Department of Transportation (DOT) and Pipeline Research Council International (PRCI) co-sponsored project using specimens taken from American Petroleum Institute (API) 5L X100 pipes [3] with an outer diameter 36 in (914 mm) and a wall thickness of 19.1 mm. The present study is motivated by the arguably surprising conclusion in [2,4,5] that better predictions can be made from toughness data extracted from Charpy V-notch (CVN) tests compared with fracture mechanics tests using single-edge-notched tensile (SE(T)) specimens. In this work, the *J*-integral is employed to describe driving and resistance forces rather than the CTOD used previously [2,4,5]. Small-specimen toughness data is used to make numerical predictions of full-scale CWP specimens, based on instability and initiation limit state methods. Several important factors that impact the utility of the *J*-integral approach are addressed. These include applicability of “apparent” *J*-integral in gross plasticity, consistency of the flaw constraint conditions in resistance curve measurements and CWP tests, the type of stress-strain relationships used, shape of the flaw, and mechanical properties at the flaw tip. The *J*-integral approach is shown to yield predictions that agree better with experimental measurements than previous CTOD-based calculations. Other factors favouring *J* over CTOD include simpler instrumentation and interpretation of small-scale tests (single-gauge versus dual-gauge set-up), avoiding the controversy over the definition of CTOD, and general applicability with no limitation of steel grade.

## CONTENTS

	<b>Page</b>
DISCLAIMER	I
EXECUTIVE SUMMARY	1
1. NOMENCLATURE	3
2. INTRODUCTION	3
2. STRUCTURE OF THE TSC PREDICTION APPROACH	4
3. DEVELOPMENT OF CWP DRIVING FORCE CURVES	7
2.1 Material model and properties	7
2.2 Calculation of $J$ -integrals in CWP specimens	9
2.3 Finite Element models for geometry factor $\eta$	11
2.4 Obtaining $J_D$ curves for CWP specimens	14
3. CWP MEASUREMENTS	15
3.1 Test description	15
3.2 Post-processing of raw test data	17
3.3 Interpretation of experimental measurements	18
4. RESULTS AND DISCUSSION	19
4.1 Treatment of inhomogeneities in prediction of the TSC	19
4.2 Predictions of TSC in CWP specimens	20
4.3 Applicability of Charpy toughness in predictions of TSC	24
5. CONCLUSIONS	26
ACKNOWLEDGEMENTS	27
REFERENCES	27
APPENDIX A. EXPERIMENTAL MEASUREMENTS OF CWP TESTS	29

## 1. NOMENCLATURE

$a$	flaw depth
$c$	flaw half-length
$t$	pipe or curved wide plate (CWP) wall thickness
$W'$	arc width of CWP specimen
$W$	width of SE(T) specimen
$H$	height of SE(T) specimen
$L$	length of CWP
$R$	outer radius of CWP
$E$	Young's modulus of elasticity
$\nu$	Poisson's ratio
$\sigma_y$	yield stress (engineering)
$\sigma_u$	ultimate stress (engineering)
$\sigma$	true stress
$\sigma_{\text{eng}}$	engineering stress
$\varepsilon$	true strain
$\varepsilon_{\text{eng}}$	engineering strain
$e$	remote engineering strain $\approx$ applied (nominal) engineering strain
$\varepsilon_u$	engineering strain at ultimate stress $\sigma_u$
$n$	strain-hardening exponent
$T$	temperature
$J_D$	$J$ -integral driving force
$J_R$	$J$ -integral resistance force
$K$	stress intensity factor
$\eta$	geometry factor

## 2. INTRODUCTION

This report revisits previous numerical predictions and experimental measurements of tensile strain capacity in curved wide plate (CWP) specimens. The tests [1,2] were under a U.S. Department of Transportation (DOT) and Pipeline Research Council International (PRCI) co-sponsored project using specimens taken from American Petroleum Institute (API) 5L X100 pipes [3] with outer diameter 36 in (914 mm) and wall thickness 19.1 mm. A detailed description of the specimens' geometry and test procedure may be found in [1]. Ductile instability and initiation limit state solution methods were presented in [4–6] to numerically predict the tensile strain capacity (TSC) of CWP specimens. The present study is motivated by the arguably surprising conclusion in [2,4,5] that better predictions can be made from toughness data extracted from Charpy V-notch (CVN) tests compared with fracture mechanics tests using single-edge-notched tensile (SE(T)) specimens. In this work, the  $J$ -integral is employed to describe driving and resistance forces rather than the crack-tip opening displacement (CTOD) used previously [2,4,5]. Small-specimen toughness data is used to make numerical predictions of full-scale CWP specimens, based on instability and initiation limit state methods. Several important factors that impact the utility of the  $J$ -integral approach are addressed. These include applicability of  $J$ -integral in gross plasticity, consistency of the flaw constraint conditions in resistance curve measurements and CWP tests, the type of stress-strain relationships used, shape of the flaw, and mechanical properties at the flaw tip. The present  $J$ -integral approach is shown to yield predictions of

TSC based on ductile instability and initiation limit state methods that agree better with experimental measurements than previous CTOD-based calculations. Strain-based design using  $J$ -integral is thus validated, supporting first-principles estimation of initiation and instability strains using only small-scale SE(T) data and  $J$ -integral calculations for CWP. Further FEA is not required, notably in the difficult simulation, post-processing, and material-specific FEA, to get CTOD predictions. Additionally, the  $J$ -integral approach avoids controversy over the definition of CTOD and the empirical conversions of CVN-to-CTOD data. Other factors favouring  $J$ -integral over CTOD include simpler instrumentation and interpretation of small-scale tests (single-gauge versus dual-gauge set-up) and general applicability with no limitation of steel grade. A review of tensile strain capacity prediction models and experimental data for strain-based design of pipelines has been presented by Park and Gianetto [7]. The paper identifies several of the gaps and issues with existing methodologies and highlights the merits of  $J$ -integral approach to TSC prediction.

This report is organized as follows. After this short introduction, Section 2 presents a brief description of the ductile instability and initiation limit state solutions along with details regarding the choice of resistance curves used in the numerical predictions. Section 3 presents details of  $J$ -integral calculations in CWP specimens and the construction of driving force curves. The previously measured CWP test data are re-analyzed in Section 4 including a discussion on the interpretation of measured remote strains and their relations to the pipe TSC. Comparisons between numerical predictions and experimental measurements are presented in Section 5 to draw conclusions on the usefulness of the prediction framework presented. Finally, Section 6 summarises concluding remarks.

## 2. STRUCTURE OF THE TSC PREDICTION APPROACH

Ductile instability and initiation limit state solution methods as described in [5,6] can be employed to estimate strain capacities of the CWP specimens. The ductile instability limit state solution method using the  $J$ -integral as fracture mechanics parameter is schematically shown in Figure 1. In this method, the limit state is defined by the tangency point of the crack driving force curve and the fracture toughness (resistance) curve. Different measures can be used to characterize driving “force” and resistance, the most common being CTOD and  $J$ -integral. Previous studies on CWP limit state strain have used CTOD [2,4–6]. In the present work, the  $J$ -integral is used because of its simpler experimental measurement as compared to CTOD. The  $J$ -integral resistance curve ( $J_R$  as a function of crack growth  $\Delta a$ ) is a function of material and test conditions (temperature, strain rate, and geometry). The  $J$ -integral driving force ( $J_D$ ) is a measure of the energy available to create new surfaces by way of crack growth. It is a function of the applied strain  $e$  and the length of the crack  $a$  (or, equivalently, crack growth  $\Delta a$ ). The *ductile instability* limit state (*i.e.*, the tensile strain capacity (TSC) and corresponding crack growth at unstable failure) is obtained by solving the following system of equations for  $e$  and  $\Delta a$ :

$$\left\{ \begin{array}{l} J_D(e, a_0 + \Delta a) = J_R(\Delta a) \\ \frac{\partial J_D(e, a_0 + \Delta a)}{\partial \Delta a} = \frac{dJ_R(\Delta a)}{d\Delta a} \end{array} \right. \quad (1)$$

where  $a_0$  is the initial length of the crack and  $e$  is the remote strain.

The *initiation* limit state is intended to give a conservative estimate of the strain capacity of the plate. It is given by the strain at which the driving force  $J_D$  of the initial (stationary) flaw reaches the initiation fracture toughness defined to be the  $J_R$  value at a small amount of crack growth  $\Delta a_{init}$ . The following equation is solved for  $e$ :

$$J_D(e, a_0) = J_R(\Delta a_{init}) \quad (2)$$

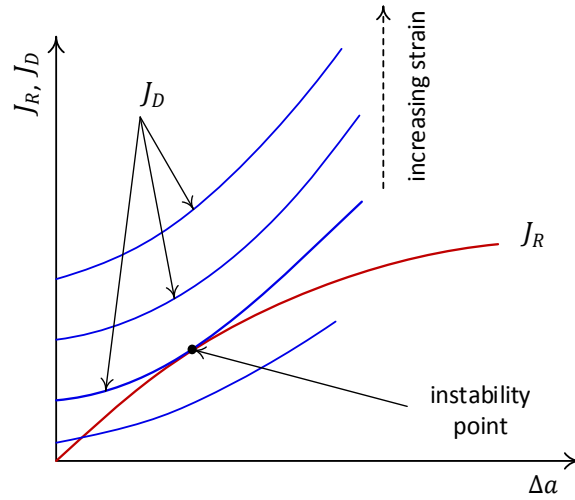


Figure 1. Schematic of the ductile instability limit state solution method. Reproduced from [5].

In practice, the specific value of  $\Delta a_{init}$  is chosen based on engineering judgment. Potential candidates often used in the literature are 0.5 mm [4] or 0.2 mm [8]. This choice will be further discussed later in Section 4.

For a meaningful comparison of  $J_R$  values with  $J_D$  values, the constraint conditions of the flaw in the small-scale specimen should be the same as those in the large-scale specimen (see also the discussion in Section 2.2 below). Shen et al. [9] concluded that the constraint in a SE(T) specimen with ratio of span between load points to width ( $H/W$ ) equal to 10 provides a reasonable match to that for a circumferential crack in a pipe of the same thickness (*i.e.*, pipe wall thickness  $t$  equal to SE(T) specimen width  $W$ ) subject to tensile loading. Resistance  $J_R$  curves previously reported in [10] for X100 pipe girth welds have been used in the present study. These curves were obtained using SE(T) specimens with  $W=17.2$  mm and  $H/W=10$  based on the test procedures detailed in [11]. For specific information regarding the material, specimen preparation and testing performed, the reader is referred to [10]. A comparison between the resistance curves obtained from SE(T) and CWP tests has been presented in [10]. Obtaining “clean” resistance curves from CWP tests is difficult owing primarily to the difficulty in measuring crack size (*i.e.*, from poor sensitivity and scatter in experimentally measured compliance) especially at initial stages of the test. Thus, comparison of resistance curves in the two geometries (CWP and SE(T)) must be considered tentative at best. By using the SE(T) resistance curves to predict the TSCs of CWP specimens, this study sheds some light on the transferability of resistance curves obtained from small scale specimens to larger scales.

The  $J_R$  curves reported in [10] include results with flaws in base metal (BM), heat affected zone (HAZ) and weld metal (WM) of the pipe girth welds. A matrix of different SE(T) specimens was created for two weld rounds with different target flaw depths, flaw locations, and test temperatures. A power law equation of the form  $J_R = c_1(\Delta a)^{c_2}$  was used for curve fitting the experimentally measured  $J_R$  curves. In each case, the corresponding curve fitting parameters  $c_1$  and  $c_2$  were reported along with comparisons of the measured and target flaw lengths. The initial flaw depths in SE(T) and CWP specimens are not necessarily equal to the targeted values (in some cases, they show more than 100% difference). In addition, the width of the SE(T) specimen was  $W = 17.2$  mm, which is marginally different than the thickness of the CWP specimens ( $t=19.1$  mm). The following procedure was applied

to restore consistency of flaw-tip constraint conditions in SE(T) and CWP specimens. The curve-fitting coefficients were first made functions of the initial flaw depth by applying a linear best fit to measured SE(T) data. The linear best-fit coefficients are summarized in Table 1-Table 3. For each CWP test, an equivalent SE(T) flaw-depth was then obtained by requiring that  $a_0^{\text{SE(T)}}/W = a_0^{\text{CWP}}/t$ . Given  $a_0^{\text{CWP}}$ , the coefficients  $c_1$  and  $c_2$  required to construct the  $J_R$  curve were obtained using an equivalent SE(T) flaw-depth of  $a_0^{\text{SE(T)}} = a_0^{\text{CWP}}W/t \approx 0.9 a_0^{\text{CWP}}$ . Note that the  $J_R$  curve data corresponding to  $-40^\circ\text{C}$  were not available in a number of cases, for example, in HAZ flaw locations in round 2. In such cases, which are highlighted in grey in the Tables, the data corresponding to either weld round 1 or temperature  $-40^\circ\text{C}$  were used instead depending on which data was available. All tests were performed at quasi-static rate.

Figure 2 shows a comparison of  $J_R$  curves corresponding to different flaw regions and crack sizes. In the following section, a scheme is developed for determining the  $J_D$  curves to enable numerical predictions of strain capacities based on ductile instability and initiation limit states.

Table 1.  $J_R$  curve-fit parameters for HAZ flaw location

		$c_1(a) = \alpha_1 + \beta_1 a$		$c_2(a) = \alpha_2 + \beta_2 a$	
		$\alpha_1$	$\beta_1$	$\alpha_2$	$\beta_2$
Round 1	23°C (RT)	1718	-95.49	0.782	-0.03643
	-20°C	1604	-99.62	0.7609	-0.007769
	-40°C	1071	91.42	1.43	-0.2121
Round 2	RT	1367	-69.85	1.117	-0.08521
	-20°C	1292	-50.2	0.8103	0.003281
	-40°C	1071	91.42	1.43	-0.2121

Table 2.  $J_R$  curve-fit parameters for WM flaw location

		$c_1(a) = \alpha_1 + \beta_1 a$		$c_2(a) = \alpha_2 + \beta_2 a$	
		$\alpha_1$	$\beta_1$	$\alpha_2$	$\beta_2$
Round 1	23°C (RT)	779.1	-35.91	0.4721	0.03978
	-20°C	730.4	-37.5	0.7345	0.004632
	-40°C	-908	430.5	-2.197	0.875
Round 2	RT	631.4	2.799	0.5221	0.04353
	-20°C	348.5	50.45	0.9948	-0.03426
	-40°C	-908	430.5	-2.197	0.875

Table 3.  $J_R$  curve fit parameters for BM flaw location

		$c_1(a) = \alpha_1 + \beta_1 a$		$c_2(a) = \alpha_2 + \beta_2 a$	
		$\alpha_1$	$\beta_1$	$\alpha_2$	$\beta_2$
Rounds 1 & 2	23°C (RT)	1445	-46.88	1.043	-0.07077
	-20°C	1648	-49.21	1.194	-0.1123
	-40°C	1648	-49.21	1.194	-0.1123

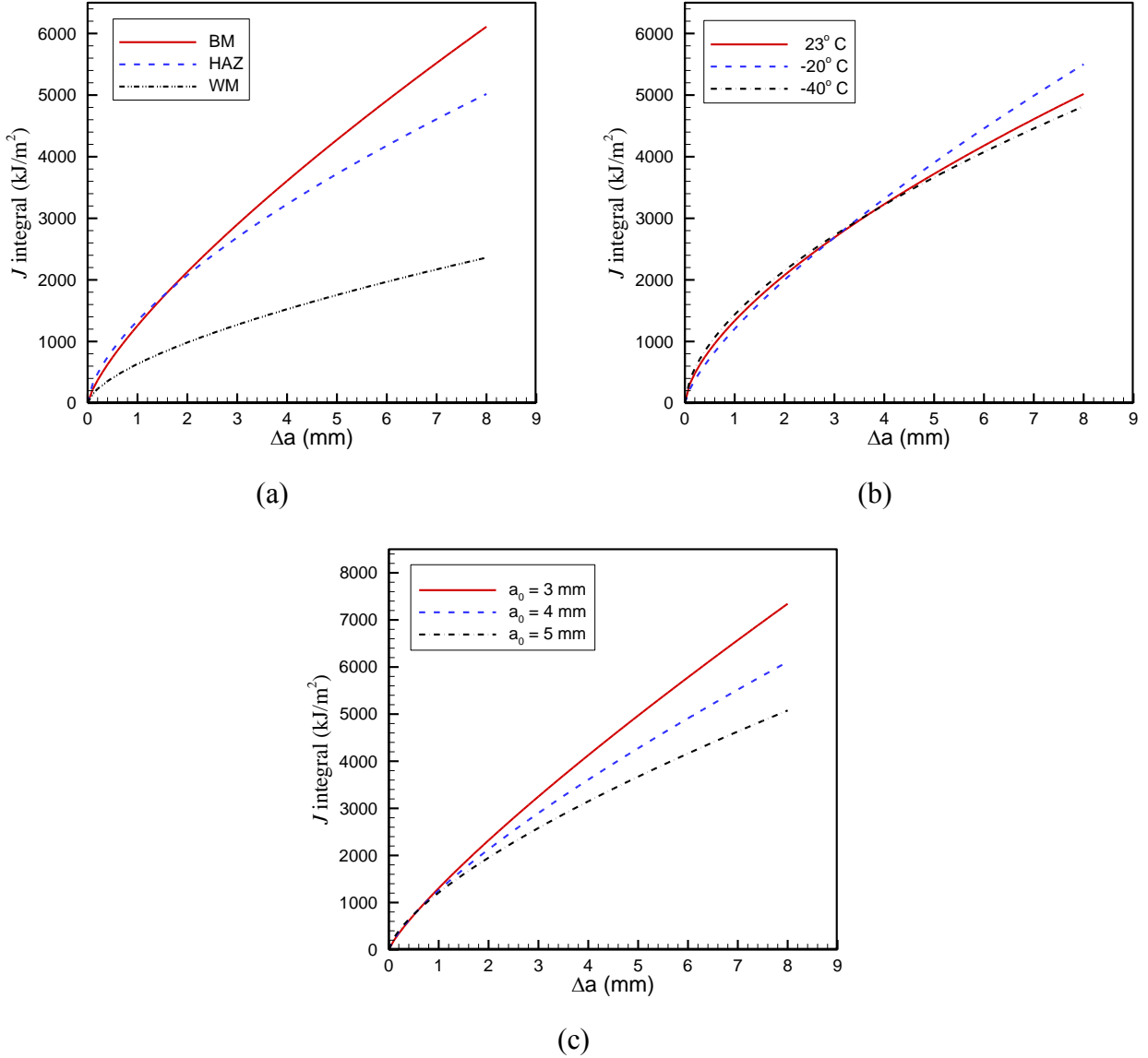


Figure 2. a)  $J_R$  curves for BM, WM and HAZ at room temperature: round 1,  $a_0/W = 4/17.2$  (i.e., 0.23), b)  $J_R$  curves (HAZ) for various temperatures:  $a_0/W = 4/17.2$  (i.e., 0.23), and c)  $J_R$  curves (BM) for various initial flaw depths at room temperature

### 3. DEVELOPMENT OF CWP DRIVING FORCE CURVES

#### 2.1 Material model and properties

The material model used was the same as in the development of SE(T) resistance curves by CANMET [11]:

$$\varepsilon = \begin{cases} \frac{\sigma}{E} & \sigma < \sigma_y \\ \frac{\sigma_y}{E} \left( \frac{\sigma}{\sigma_y} \right)^n & \sigma \geq \sigma_y, \end{cases} \quad (3)$$

where  $\varepsilon$  and  $\sigma$  are the *true* strain and *true* stress, respectively,  $E$  is the Young's modulus,  $\sigma_y$  is the yield strength, and  $n$  is the strain-hardening exponent. In all cases, elastic properties were  $E = 206.7$  GPa and  $\nu = 0.3$ . Note that as opposed to the material model found in CSAZ662, *i.e.*,

$$\varepsilon_{\text{eng}} = \frac{\sigma_{\text{eng}}}{E} + \left(0.005 - \frac{\sigma_y}{E}\right) \left(\frac{\sigma_{\text{eng}}}{\sigma_y}\right)^{n_{\text{CSA}}}, \quad (4)$$

the material model equation (3) is written in terms of true stresses and strains. Note that the CSAZ662 equation is valid only for stresses up to the ultimate engineering stress  $\sigma_u$ . The post- $\sigma_u$  stress-strain behaviour is sometimes assumed to follow a constant (flat) curve [5]. Some authors have used the CSAZ662 equation (4) presumably extrapolated beyond the ultimate stress, see *e.g.*, reference [12].

Table 4 summarizes the CANMET model tensile properties considered for the pipe base metal (X100), HAZ, and weld metal in the present study. The strain-hardening exponent  $n$  was obtained by converting those given in [4] based on the CSAZ662 model by requiring that the engineering strains at engineering ultimate stress obtained from the two models are equal. It should be noted that, in addition to pipe-to-pipe strength variation, there is a considerable range of yield stress values associated with circumferential location even on a single pipe [13]. Hence, the properties given in Table 4 should only be regarded as representative properties of the X100 steel.

Note that the type of the stress-strain model employed can significantly impact  $J$ -integral values. Figure 3 shows a comparison of  $J$ -integrals of a semielliptical flaw of  $a/t = 5/19.1$  (0.26) and  $2c/t = 50/19$  (2.63) in the CWP obtained using the CANMET model equation (3) and CSAZ662 model equation (4). In implementing the CSAZ662 model, the true stresses were obtained by converting the engineering values in equation (4) up to the engineering stress of  $\sigma_u$  and kept constant at higher strains. The difference observed in the  $J$ -integral values reaches 35% in this particular case. The choice of equation (3) for the material model was thus made for consistency of  $J_D$  calculations in the present work with the  $J_R$  measurements and calculations in [10,11]. As also reported in [11], the strain hardening component  $n$  has a negligible effect on  $J$ -integral values since at large values of  $n$  the strain-stress curve is nearly flat and insensitive to variations in  $n$ .

The yield strengths given in Table 4 correspond to room temperature. The constitutive equation proposed in [14,15] was used to adjust the material properties at different temperatures by adding the thermal component of the flow stress  $\Delta\sigma_{th}$  to the yield strength at room temperature and quasi-static rate:

$$\Delta\sigma_{th} = \left[27.98 - 0.00393 T \ln\left(\frac{10^8}{\dot{\varepsilon}}\right)\right]^2, \quad (5)$$

where  $T$  is the temperature in Kelvin and  $\dot{\varepsilon}$  is the strain rate in 1/s. Since all CWP tests were conducted in quasi-static conditions, the strain rate was taken to be very low at  $\dot{\varepsilon} = 1 \times 10^{-3}$ /s in all cases. The thermal stress according to equation (5) over the range of temperatures in this work is very small; at  $T = -20^\circ\text{C}$ , the thermal stress is only about 7 MPa.

Table 4. Tensile properties (longitudinal) of different regions of X100 pipe in CWPs

		Tensile Properties	
		$\sigma_y$	$n$
Base Metal & HAZ		781	17.32
Weld metal	Round 1	835	16.10
	Round 2	827	19.61

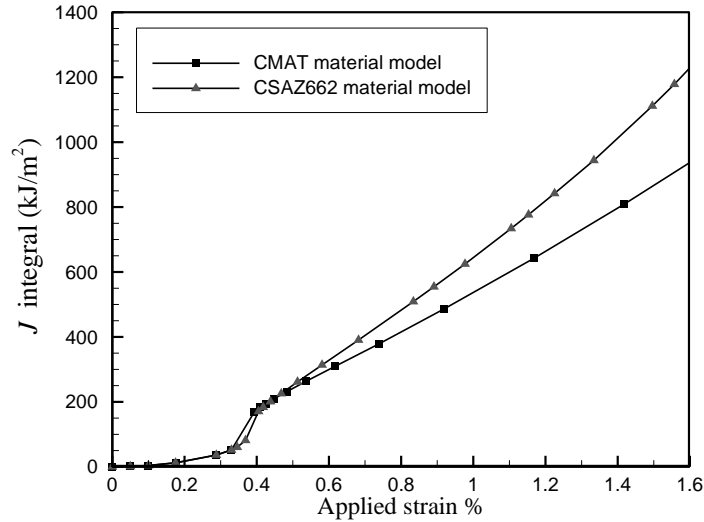


Figure 3. Comparison of  $J$ -integrals of a semielliptical flaw of  $a/t = 5/19.1$  (*i.e.*, 0.26) and  $2c/t=50/19$  (*i.e.*, 2.62) in a CWP obtained using the CANMET and CSAZ662 material models. Applied strain: displacement divided by the specimen length ( $2L$ ); see Figure 6.

## 2.2 Calculation of $J$ -integrals in CWP specimens

In incremental plasticity, path independent  $J$ -integrals can only be obtained under small scale and contained yielding conditions and provided that contour integrals used in the calculations are large enough to surround the plastic zone and pass through the elastic region only [16]. In practice, it is advised to consider as many contour integrals as possible to ensure that the “saturated value” of  $J$  is reached in the limit of increasing contour size. In the CWP specimens used in this work, this is not possible since gross plasticity is encountered for the loading levels of interest. In that case, path dependence increases strongly and a saturated value of  $J$  cannot be reached. An example of this situation is shown in Figure 4. The calculated contour integrals become increasingly path dependent as the strain increases so that a saturated value cannot be obtained beyond approximately 1.1% of applied strain.

Loss of path dependence in this case may be viewed as being equivalent to deviation from an HRR-like stress field in nonlinear elasticity theory as “constraint” is lost, *i.e.*, as excessive plastic deformation occurs. To ensure small scale yielding and high constraint, the ASTM test standard E1820 [17] specifies a maximum  $J$ -integral capacity (validity range) for bend fracture mechanics specimens given by the smaller of  $\sigma_y(t - a_0)/10$  and  $\sigma_y B/10$  where  $B$  is the specimen thickness. It is generally accepted that constraint is lower in tension specimens than in bending specimens so the above limits would be even tighter (smaller validity range) for SE(T) specimens. In two-parameter fracture mechanics, this limitation is addressed by calculation of a second parameter to ensure that the constraint is the same in the specimen as in the application. For example, Shen et al. [9] used the parameter  $Q$  to demonstrate that crack-tip conditions are the same in the SE(T) specimen and pipe application. They compared the SE(T) test specimen behaviour with that of a circumferential crack in a pipe to show that the specimen geometry used for SE(T) testing (clamped specimen,  $H/W=10$ ) was adequate to ensure equivalent constraint ( $J - Q$  match) as  $J$  values increased. Similarly, for CWPs it is stipulated that the constraint conditions at the flaw-tip should remain equivalent to those of the SE(T) geometries as  $J$  increases beyond the validity range to generate an HRR-like stress field.

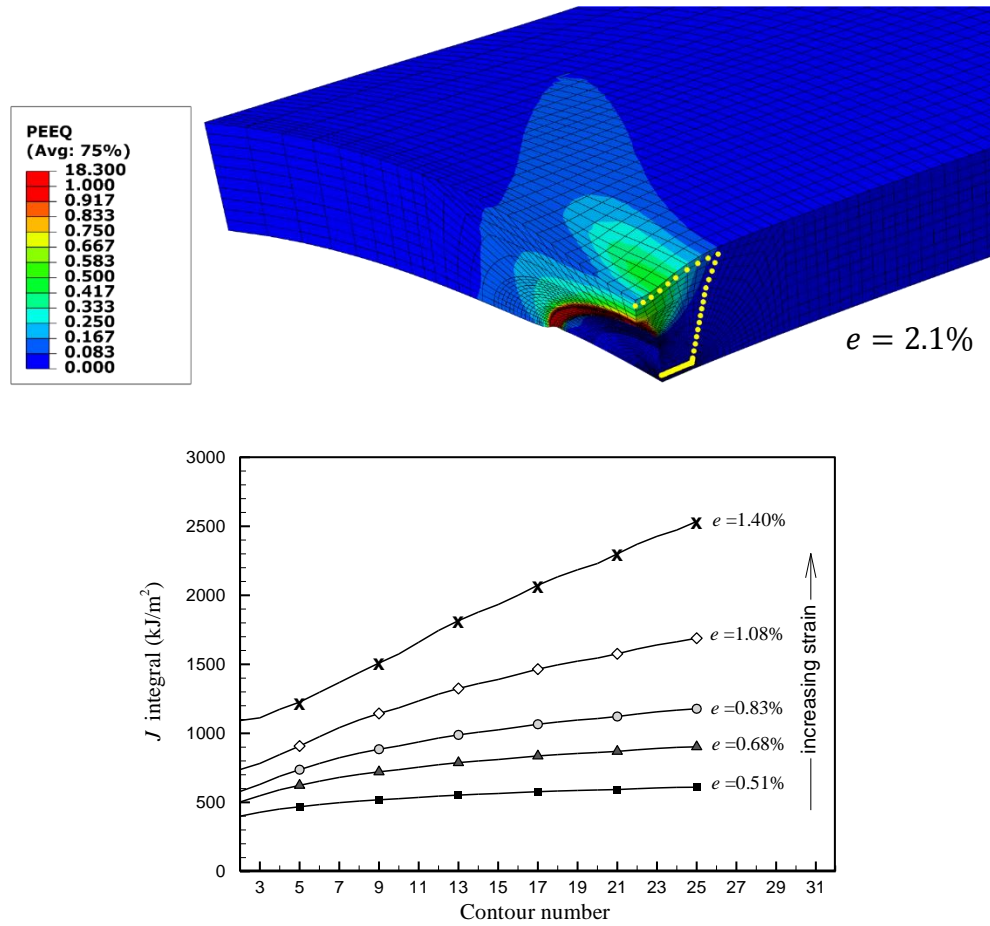


Figure 4. An example of loss of path dependence of  $J$  owing to reaching gross plasticity. Only a quarter of the plate is shown. The yellow circles in the top figure mark the boundary of the largest contour integral domain (contour number 25). Note that the contour integral cannot touch the free surface, otherwise  $J$  calculations are not valid [16]. Flaw size  $a/t=8/19.1$  (*i.e.*, 0.42),  $2c/t=50/19.1$  (*i.e.*, 2.62). BM properties were used (see Table 4)

With these considerations in mind, the method used in the present study to circumvent the issues emanating from excessive plastic deformation (*i.e.*, strong path dependence of  $J$ -integrals and loss of constraint) is as follows. The plastic component of  $J$ -integral is evaluated as a function of area under the load versus plastic CMOD curve and added to the well-established elastic component (see equation (6) below) based on the method in ASTM E1820 [17]. Parameters are obtained using the procedure described in [12] for small scale, contained plasticity in which  $J$ -integral values obtained from direct contour integral calculations are valid. At larger strains where gross plasticity is encountered,  $J$ -integral values are calculated from the developed relationship rather than direct contour integral calculations. This method of calculating  $J_D$  integrals is similar to that used in calculating  $J_R$  curves and ensures that the same definitions of  $J$ -integral, whatever they mean, are being calculated in constructing  $J_D$  and  $J_R$  curves throughout the course of loading. Given that the constraint conditions in SE(T) and CWP specimens (*i.e.*,  $a/W$  and  $a/t$ , respectively) have been designed to be similar (see also Section 2), the calculated  $J$ -integral values provide a parameter that describes the same crack-tip conditions in the small-scale test and the CWP application. As such,  $J$ -integral can be used in estimating the TSCs even

though it strictly loses its validity in gross plasticity *i.e.*, its single-parameter ability to characterize the crack-tip stress state. In that sense,  $J_D$  and  $J_R$  integrals here may be viewed as “apparent” values.

The formula for determining  $J$  from load versus plastic CMOD data for a stationary crack in a CWP is [17]

$$J = J_e + J_{pl} = \frac{K^2(1 - \nu^2)}{E} + \frac{\eta A_{pl}}{W'(t - a)}, \quad (6)$$

in which  $K$  is the stress intensity factor in the elastic regime which is taken to be equal in semielliptical and canoe-shape flaws [18] and is given in [2,19],  $\nu$  is Poisson’s ratio,  $E$  is Young’s modulus,  $W'$  and  $t$  are the specimen arc-width and thickness, respectively,  $a$  is the flaw depth and  $A_{pl}$  is the area under the load versus plastic CMOD curve as described in [17]. The geometry factor  $\eta$  depends only on the specimen geometry (including the flaw shape, *e.g.*, semielliptical or canoe shape). Note that  $\eta$  is independent of mechanical properties. An expression for  $\eta$  for semielliptical flaws in CWP specimens is given in [12] using the CSAZ662 material model.  $\eta$  will be calculated in Section 2.3 using the CANMET stress-strain material model, see equation (3).

Consider again the semielliptical flaw of Figure 4. The  $J$ -integral values obtained from the largest contour domain and from plastic load versus CMOD and  $\eta$  are compared in Figure 5. The calculated values begin to diverge as soon as path independence is lost (at approximately 1.1% strain). At higher strains, the contour integral calculations pass through a maximum and begin to decrease (not shown in the figure), a physically unacceptable behaviour that appears to be a direct consequence of loss of path dependence.

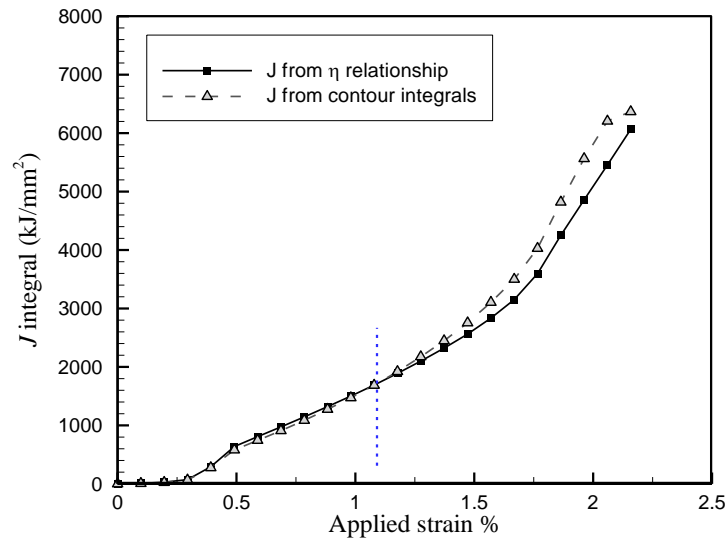


Figure 5. Comparison of  $J$  values calculated from contour integrals and  $\eta$  relationship (*i.e.*, plastic load versus CMOD) for a flaw with  $a/t=8/19.1$  (*i.e.*, 0.42) and  $2c/t=50/19.1$  (*i.e.*, 2.62). BM properties were used. See also Figure 4.

### 2.3 Finite Element models for geometry factor $\eta$

The geometry factor  $\eta$  was determined using finite element simulations performed using Abaqus Standard [20]. The target flaw profile in the experimental procedures has been reported to be an arc matching the inside diameter of the pipe (*i.e.*, canoe shape). Because the flaws are extended in fatigue

to sharpen the tip, the geometry of the flaws produced in practice vary in shape somewhat as opposed to being strictly semielliptical or canoe-shape. In the following, both semielliptical and canoe-shape flaw geometries are considered to assess their effect on  $J$ -integral values. A typical finite element (FE) model of a CWP specimen along with a schematic of the flaw shape in each case is shown in Figure 6.

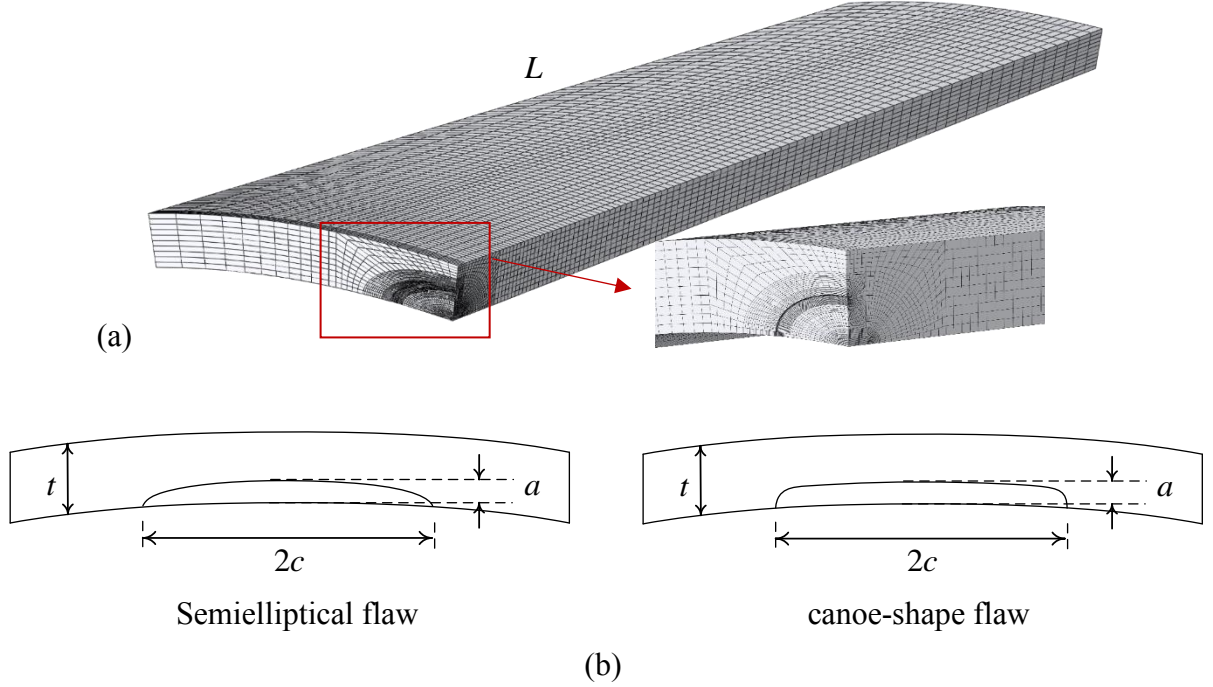


Figure 6. a) Typical Finite Element model of a CWP (only a quarter of the plate is modelled to take advantage of symmetry), and b) schematic of semielliptical and canoe-shape flaws

The matrix of FE simulations considered for obtaining  $\eta$  is defined by  $a \in \{2,3,4,5,6,7,8,9\}$  mm,  $2c \in \{30,50,75\}$  mm and  $\sigma_y \in \sigma_y(\{\text{HAZ, WM, BM}\} \times \{\text{weld round 1 \& 2}\})$ . Only a quarter of the plate was modelled to exploit the plate symmetry. An increasing displacement was applied in the longitudinal direction at the free end while the symmetry plane was constrained in a way consistent with the symmetric deformation. The total displacement applied in each case was large enough to induce sufficient plastic deformation at the crack tip without undermining the “nearly-contained plasticity” conditions in view of the discussion in Section 2.2. It was confirmed that the “saturated” value of  $J$  was reached by verifying that the values obtained from the three largest contour integrals differed by no more than 5% (see Figure 4).

With  $J_{pl} = J - J_e$  obtained from FEA,  $\eta$  was then taken to be the slope of the best linear fit to  $J_{pl}$  versus  $A_{pl}/W'(t - a)$  data points obtained at various load levels. Having  $\eta$  for all combinations of  $a/t$  and  $2c/t$ , a curve fitting approach similar to the one in [12] was conducted leading to

$$\eta\left(\frac{a}{t}, \frac{2c}{t}\right) = 0.2246 + 0.3338\left(\frac{a}{t}\right) - 1.7198\left(\frac{a}{t}\right)^2 + 0.2270\sqrt{\ln\left(1 + 8.0622\frac{2c}{t}\right)}, \quad (7)$$

for a semielliptical flaw shape and

$$\eta\left(\frac{a}{t}, \frac{2c}{t}\right) = 0.7095 + 0.4269\left(\frac{a}{t}\right) - 1.6236\left(\frac{a}{t}\right)^2 - 0.0944\sqrt{\ln\left(1 + 8.0679\frac{2c}{t}\right)}, \quad (8)$$

for a canoe shape flaw.  $J$ -integrals used in the construction of  $J_D$  curves were calculated from equations (6)-(8) (and not the contour integral calculations) in which the plastic load versus CMOD data were obtained from FEA. Figure 7(a) compares the variation of  $\eta$  with  $a/t$  at fixed  $2c/t = 50/19.1$  (*i.e.*, 2.62) for the semielliptical and canoe-shape flaws. Furthermore, typical evolution of  $J$  with applied strain for semielliptical and canoe-shape flaws of  $a/t = 5/19.1$  (*i.e.*, 0.26) and  $2c/t = 50/19.1$  (*i.e.*, 2.62) are shown in Figure 7(b). The  $J$ -integrals shown were obtained from direct contour integral calculation;  $J$  values obtained from load versus plastic CMOD data were practically identical and are not shown for brevity of presentation. The  $J$ -integral values are equal in the elastic range (initial quadratic part of the curves). However, they begin to diverge as plastic strains increase in the ligament. The difference is approximately 20% in this particular case. At applied strain of 1.5%, the value of  $A_{pl}/(W'(t-a))$  is 1834.6 N/mm in the canoe-shape flaw whereas it is 1357.8 N/mm in the semielliptical flaw, *i.e.*, the plastic CMOD is significantly higher in the canoe-shape flaw. This is reflected in higher total values of  $J$ -integral for the canoe-shape flaw:  $J_{pl} = 1005.4$  kJ/m<sup>2</sup> in the canoe-shape flaw whereas  $J_{pl} = 823.5$  kJ/m<sup>2</sup> in the semielliptical flaw ( $J_e$  is approximately 73.5 kJ/m<sup>2</sup> in both cases). These difference lead to as high as 20% difference in  $\eta$  over the range of strain shown in Figure 7 with the  $\eta$  values being lower for the canoe-shape flaw.

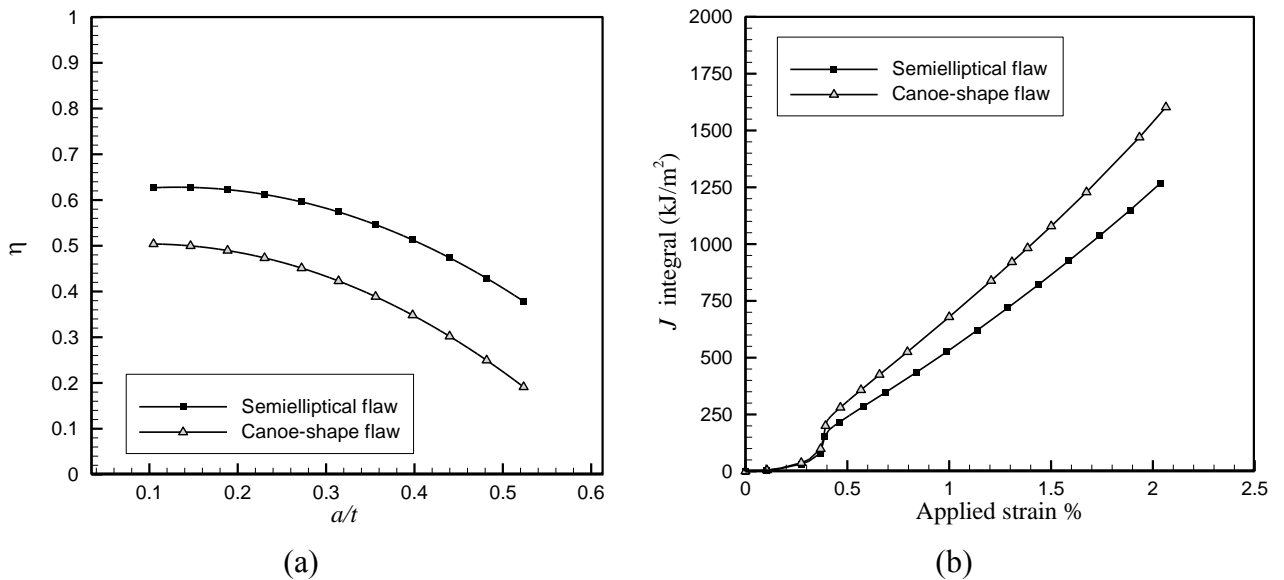


Figure 7. a) Variation of  $\eta$  with  $a/t$  for semielliptical and canoe-shape flow geometries with  $2c/t = 50/19.1$  (*i.e.*, 2.62), b) variation of  $J$ -integrals with applied strain for a canoe-shape and semielliptical flow with  $a/t = 5/19.1$  (*i.e.*, 0.26) and  $2c/t = 50/19.1$  (*i.e.*, 2.62). BM properties were used. Applied strain is defined as the end displacement divided by the specimen length  $L$  (Figure 6).

Given the uncertainties in the flaw shape, a certain level of error is inevitable in  $J$ -integral calculations. Semielliptical flaw geometries have been employed in most works in the literature (see *e.g.*, [5,21]) and are assumed to represent the actual flaw geometry in the remainder of this study.

The  $J_D$  integrals were obtained assuming uniform material properties to simplify the model. This introduces a certain level of approximation since CWP specimens are in fact inhomogeneous and the flaw-tip plastic strains extend into the other regions neighbouring the flaw-tip location. Further details on how inhomogeneity is addressed in the calculations of  $J_D$  will be presented in Section 4.

## 2.4 Obtaining $J_D$ curves for CWP specimens

The  $J_D$  curves represent evolution of  $J$ -integral as a function of applied strain and crack growth. Such relationships are derived by interpolating  $J$ -integral values obtained for stationary cracks of different sizes. As such, the underlying assumption is that, at a given applied strain,  $J$ -integral depends only on the current size of the crack and not on its propagation history.

The  $J$ -integral in the elastic-plastic regime is assumed to have the following general form:

$$J = J(a, c, t, R, \sigma_y, n, e). \quad (9)$$

Applying standard dimensional analysis, the dimensionless parameters involved are  $J' = J/\sigma_y t$ ,  $a/t$ ,  $2c/t$ ,  $R/t$ ,  $n$ , and  $e$ . Given that  $R/t$  is constant in the present application, the above equation is written in dimensionless form as

$$J' \equiv \frac{J}{\sigma_y t} = f\left(\frac{a}{t}, \frac{2c}{t}, n, e\right). \quad (10)$$

Note that  $J$  in general varies quadratically with the applied strain (which is taken to be equal to the remote strain  $e$ ) when the pipe deformation is elastic with confined plasticity at the flaw tip, and linearly when plasticity develops through the net section prior the occurrence of ligament instability. The latter is relevant to strain based design [22,23]. With that consideration in mind, the general form of  $f$  is taken to be [23]

$$f = \beta_0 + \beta_1 e, \quad (11)$$

where  $\beta_0$  and  $\beta_1$  are functions of  $a/t$  and  $n$  given by

$$\begin{aligned} \beta_0 &= \theta_1 + \theta_2 \frac{a}{t}, \\ \beta_1 &= (\theta_3 + \theta_4 n) + (\theta_5 + \theta_6 n) \left(\frac{a}{t}\right) + (\theta_7 + \theta_8 n) \left(\frac{a}{t}\right)^2. \end{aligned} \quad (12)$$

In the above,  $\theta_1, \dots, \theta_8$  are functions of  $2c/t$  given by

$$\theta_i = \alpha_{3i-2} + \alpha_{3i-1} \left(\frac{2c}{t}\right) + \alpha_{3i} \left(\frac{2c}{t}\right)^2, \quad (13)$$

where  $\alpha_{3i-2}, \alpha_{3i-1}, \alpha_{3i}$ ,  $i = 1:8$ , are interpolation coefficients. The matrix of FE simulations considered to calibrate the coefficients was the same as that used in determining  $\eta$  (see section 2.3). In each case, the applied strain was increased up to 5% so that significant plastic strain occurred in the ligament and the  $J$ -integrals were obtained using the load versus plastic CMOD data and the geometry factor obtained in the preceding section.  $\theta_i$  values were first obtained independently for each flaw length  $2c \in \{30, 50, 75\}$  mm by applying a least-square curve fitting to the  $J$  versus  $(a/t, e, n)$  data points for each  $2c$ . Only the post-elastic data points (*i.e.*, points where  $J$  varies linearly with applied strain) were considered in calibrating the coefficients. The obtained solutions were then used to express  $\theta_i$  as a function of  $2c/t$  through the second order equation (13). The results are summarized in Table 5. Caution should be taken when using approximate equations (10)-(13) for calculations outside the ranges considered in the FE matrix.

Table 5. Curve fitting coefficients for approximate  $J_D$  curves eqns. (10)-(13)

	$\alpha_{3i-2}$	$\alpha_{3i-1}$	$\alpha_{3i}$
$\theta_1$	-0.0001	0.0093	-0.0099
$\theta_2$	-0.0005	-0.056	0.0504
$\theta_3$	0.0046	-0.0275	0.0287
$\theta_4$	-0.0001	0.001	-0.0011
$\theta_5$	-0.0713	0.4193	-0.3749
$\theta_6$	0.0021	-0.0192	0.0221
$\theta_7$	0.2204	-1.2751	1.3577
$\theta_8$	-0.0068	0.0781	-0.0887

### 3. CWP MEASUREMENTS

#### 3.1 Test description

Six linear variable differential transformer (LVDT) gauges were installed in the axial direction in each specimen. A schematic of the CWP specimen together with the LVDT gauge placements is shown in Figure 8. Two pairs of LVDT gauges were placed in the “remote region” on each side of the flaw, one pair on the outer surface of the plate (gauges 1A and 1B) and the other pair on the inner surface of the plate (gauges 2A and 2B). These gauges were offset from the axial centerline to avoid the regions of “artificially” large strains owing to the design of the specimen. The remaining two LVDT gauges were placed on the edges of the plate (gauges 3A and 3B) and were to measure the “across-the-flaw” elongation. With this configuration, there isn’t a point on the specimen that lacks strain capture in the axial direction. The strains were obtained by dividing the elongations measured by the LVDT gauges by their initial lengths.

Thirty-four CWP specimens of X100 pipe were tested by NIST in the DOT/PRCI sponsored project [1,2]. Of these, the raw data of 29 tests are considered for further analysis here. These tests are summarized in Table 6. The raw data of the few remaining tests were either judged not processable (*e.g.*, CWP-15 which showed excessive noise possibly resulting from LVDT failure), were incomplete (*e.g.*, CWP-3), or were no longer available. Three flaw locations were tested, namely, BM, WM, and HAZ. Two rounds of welds were made, namely, Round 1 (single-torch mechanized GMAW process) and Round 2 (dual-torch mechanized GMAW process). The target flaw depths were 2, 3 and 6 mm and the target flaw lengths were 30, 50 and 75 mm. However, the actual flaw depths achieved (see Table 6) differed somewhat from these targets owing primarily to variable fatigue precracking increments. Table 6 also includes the remote strains measured below and above the flaw. The last three columns show the numerical prediction results obtained based on the ductile instability and initiation limit state methods. Further discussion on the meaning of these variables will be presented below.

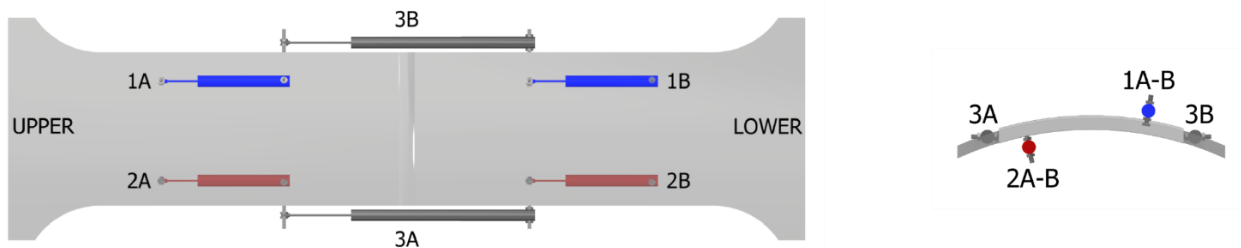


Figure 8. Schematic of the CWP along with LVDT gauge placements

Table 6. Summary of CWP specifications and measured strains (in percent). All dimensions in mm.

Specimen ID	target $a \times 2c$	Temperature ( $^{\circ}C$ )	Flaw location	Weld Round	Measured $a_0$	Measured Thickness	Remote strain below the weld	Remote strain above the weld	Measured $\Delta a$	Predicted $\Delta a$ (ductile instability)	Predicted TSC range (ductile instability)	Predicted TSC range (initiation) $\Delta a_{init} = 0.2$
CWP-BM1	3×50	-20	BM	-	3.11	19.00	3.9	4.34	1.44	[ 1.83 2.57 ]	[3.23 4.40]	[1.49 1.59]
CWP-BM2	3×50	25	BM	-	3.00	19.13	3.65	4.79	8.29	[ 1.74 2.42 ]	[3.01 4.04]	[1.44 1.53]
CWP-1	6×30	25	WM-Centerline	1	6.36	18.97	1.32	2.34	2.94	[ 2.50 3.59 ]	[1.09 1.30]	[0.81 0.81]
CWP-2	3×50	-20	HAZ-Below the weld	1	2.98	18.97	3.07	3.81	1.79	[ 1.45 1.95 ]	[2.87 3.71]	[1.67 1.73]
CWP-5	3×50	-20	HAZ-Below the weld	1	2.91	19.00	2.89	1.74	0.96	[ 1.42 1.91 ]	[2.98 3.85]	[1.75 1.81]
CWP-6	2×75	25	WM-Centerline	1	2.12	19.03	2.66	1.92	1.98	[ 0.74 0.86 ]	[2.54 2.86]	[2.13 2.08]
CWP-7	2×75	-20	WM-Centerline	1	2.23	19.10	2.31	4.23	1.67	[ 1.04 1.25 ]	[2.26 2.59]	[1.33 1.39]
CWP-8	2×75	25	HAZ-Below the weld	1	2.17	18.93	2.78	5.56	0.89	[ 0.77 0.98 ]	[3.98 4.74]	[3.10 3.19]
CWP-9	2×75	-20	HAZ-Above the weld	1	1.97	19.01	4.81	2.09	0.64	[ 0.78 0.98 ]	[4.35 5.20]	[3.06 3.23]
CWP-10	6×30	-20	HAZ-Above the weld	1	6.06	18.98	1.77	1.76	4.81	[ 3.66 5.08 ]	[1.90 2.77]	[0.76 0.78]
CWP-11	3×50	-20	WM-Centerline	1	3.14	18.96	2.44	2.62	7.6	[ 1.66 2.20 ]	[1.96 2.33]	[1.27 1.30]
CWP-12	6×30	-20	HAZ-Below the weld	1	6.14	18.90	3.22	3.71	1.82	[ 3.67 5.10 ]	[1.85 2.69]	[0.75 0.76]
CWP-13	3×50	-40	WM-Centerline	1	2.95	18.77	2.05	2.47	2.39	[ 0.80 0.94 ]	[1.45 1.61]	[1.40 1.33]
CWP-14	3×50	-40	WM-Centerline	1	3.21	18.99	2.55	2.35	2.65	[ 1.33 1.68 ]	[1.60 1.84]	[1.23 1.22]
CWP-16	3×50	25	WM-Centerline	1	3.39	18.97	2.31	2.23	8.02	[ 1.33 1.72 ]	[1.88 2.17]	[1.45 1.45]
CWP-17	3×50	-40	HAZ-Above the weld	1	3.09	18.98	2.70	2.89	0.77	[ 1.60 2.19 ]	[2.83 3.72]	[1.51 1.58]
CWP-18	3×50	-40	Weld-Centerline	1	2.81	18.84	3.97	3.15	0.85	[ 0.57 0.65 ]	[1.39 1.54]	[1.48 1.37]
CWP-19	3×50	-20	Weld-Centerline	1	3.27	18.96	2.33	2.26	1.98	[ 1.71 2.28 ]	[1.89 2.26]	[1.24 1.26]
CWP-20	3×50	25	Weld-Centerline	2	2.88	18.92	1.86	1.45	4.88	[ 1.13 1.45 ]	[1.97 2.27]	[1.54 1.55]
CWP-21	3×50	25	HAZ-Above the weld	2	3.09	18.81	1.80	1.89	2.65	[ 1.84 2.57 ]	[2.54 3.44]	[1.17 1.25]
CWP-22	3×50	-20	WM-Centerline	2	2.96	18.98	1.92	1.79	4.37	[ 1.78 2.44 ]	[1.75 2.12]	[1.00 1.05]
CWP-23	3×50	-20	HAZ-Above the weld	2	2.94	18.93	2.18	2.26	3.48	[ 1.67 2.29 ]	[2.65 3.53]	[1.32 1.39]
CWP-24	6×30	25	WM-Centerline	2	6.36	19.23	1.50	1.63	3.06	[ 4.23 6.05 ]	[1.80 2.40]	[0.91 0.93]
CWP-25	6×30	25	HAZ-Below the weld	2	6.29	19.20	1.84	1.28	2.68	[ 2.83 3.80 ]	[1.56 2.11]	[0.84 0.83]
CWP-26	6×30	-20	WM-Centerline	2	6.15	19.22	1.41	1.85	3.52	[ 4.01 5.70 ]	[1.83 2.41]	[0.94 0.96]
CWP-27	6×30	-20	HAZ-Above the weld	2	6.19	19.23	2.14	2.14	2.88	[ 4.80 6.90 ]	[2.17 3.43]	[0.65 0.68]
CWP-28	3×50	-40	WM-Centerline	2	3.08	19.17	2.21	1.93	3.17	[ 0.92 1.13 ]	[1.46 1.62]	[1.30 1.27]
CWP-29	3×50	-40	HAZ-Above the weld	2	3.35	19.14	2.53	2.58	0.99	[ 1.56 2.11 ]	[2.59 3.36]	[1.50 1.54]

### 3.2 Post-processing of raw test data

Some post-processing of the raw test data was found necessary to make full use of the information. Figure 9 shows the post-processed data of CWP-09 as a representative of the experimental measurements. For the results of the remaining tests, the reader is referred to Appendix A. The reason why postprocessing was needed is as follows. First, the specimens are always pre-loaded, and the gauges are not typically “zeroed-out” before the start of the test (in some cases a polarity issue exists as well). In addition, the geometries of CWP specimens deviate from ideal. As residual stresses are relieved when the half-plates are sectioned from the pipes, the resulting CWPs warp somewhat. If, for example, a specimen starts out warped (bent) and then straightens at higher loads then the LVDT readings will be affected, especially in the initial stages. The raw load-strain curve was moved to pass through the origin by first approximating a best fit to its elastic part and then shifting the strain values in such a way that this line passes through the origin. To do so, an algorithm was developed that uses all data points up to 0.5% strain to determine which part of the curve in this range best represents the elastic slope.

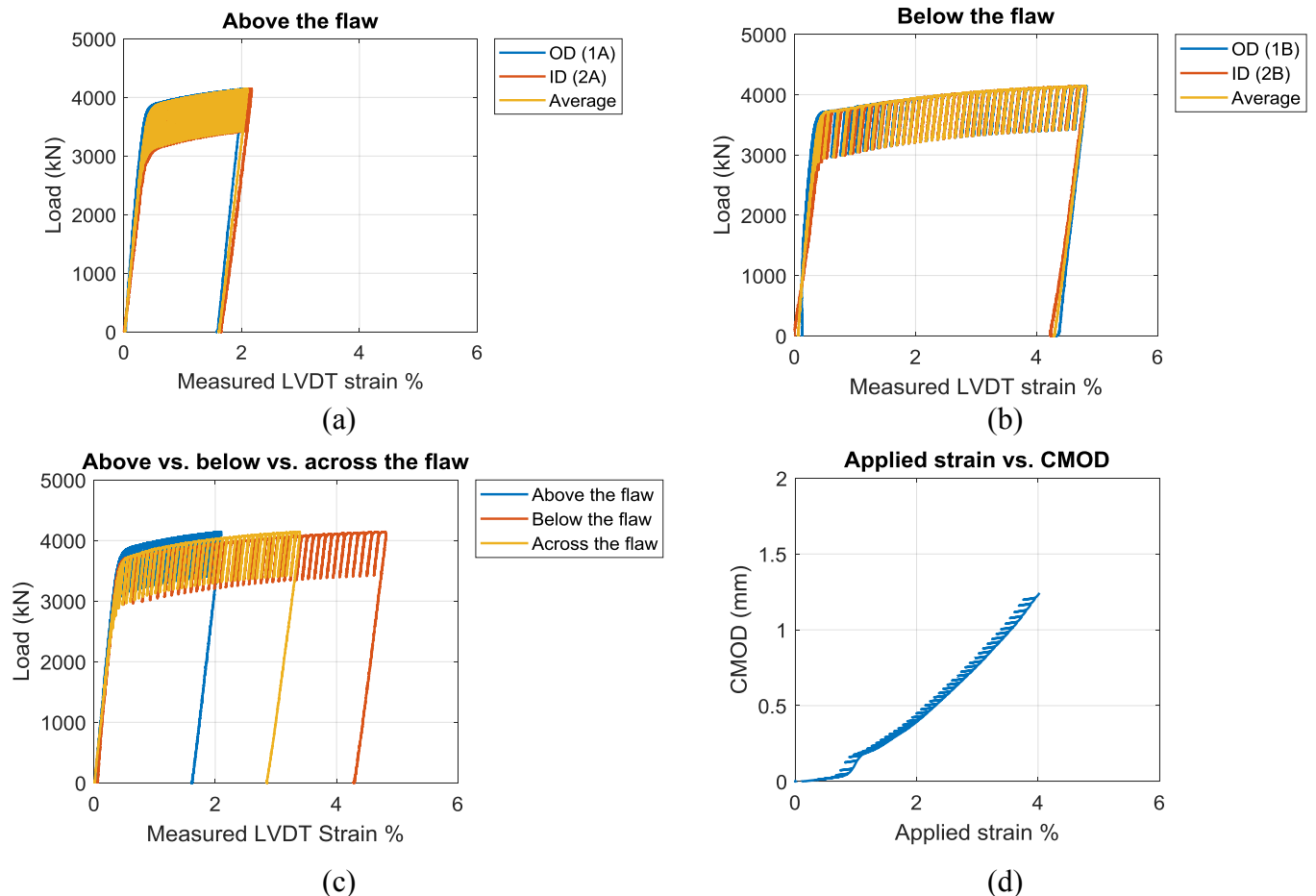


Figure 9. Post-processed data of CWP-09

The LVDT readings on the ID and OD surfaces of the plate invariably show a discrepancy especially in the elastic loading ranges. The discrepancy in the elastic range is attributed, as described above, to misalignment of the welded half-plates which causes bending (*i.e.*, non-axial strains) when the plate is subject to nominally axial loads. One expects the average of OD and ID readings measured on the two

sides of the plate to represent the axial strain. Hence, the average of OD and ID strains is taken as the value of the strain at each section along the plate. Although the strains measured above, below and across the flaw agree in the elastic range, they begin to diverge as plastic strains and crack growth develop in the specimen. An example of this is the CWP-09 test (see Figure 9(d)). A similar behaviour was observed in almost all other tests even in BM only (no weld) tests where the whole plate was taken from one pipe. On average, there is a discrepancy of ~50% between measurements above and below the flaw. This non-symmetric behaviour has been attributed to differences in the yield strengths and work hardening behaviours above and below the flaw [4]. To further clarify this, consider a simplified model of the flawed plate as shown in Figure 10. Assume purely axial (one-dimensional) deformation in the longitudinal direction. At a given load applied through the plate ends, a small difference between the stress-strain curves of the two remote regions can lead to a relatively large difference in remote strains owing to flatness (large  $n$  values) of the stress-strain curves. With the material model given in equation (3), one may deduce from the equality of nominal stresses in the remote regions above and below the flaw that

$$\sigma_y^a \left( \frac{E \varepsilon^a}{\sigma_y^a} \right)^{1/n^a} = \sigma_y^b \left( \frac{E \varepsilon^b}{\sigma_y^b} \right)^{1/n^b}, \quad (14)$$

or

$$\varepsilon^a = \frac{\sigma_y^a}{E} \left( \frac{\sigma_y^b}{\sigma_y^a} \right)^{n^a} \left( \frac{E \varepsilon^b}{\sigma_y^b} \right)^{\frac{n^a}{n^b}}, \quad (15)$$

where superscripts  $a$  and  $b$  denote the variables above and below the flaw. For  $n_a \cong n_b \equiv n$ , the above equation simplifies to

$$\frac{\varepsilon^a}{\varepsilon^b} \cong \left( \frac{\sigma_y^b}{\sigma_y^a} \right)^{n-1}. \quad (16)$$

For  $n \gg 1$ , a small difference between  $\sigma_y^a$  and  $\sigma_y^b$  translates into a large difference between  $\varepsilon^a$  and  $\varepsilon^b$  (thus between  $e^a$  and  $e^b$ ). For example, with  $\sigma_y^b/\sigma_y^a = 1.1$ , one obtains  $e^a/e^b \cong 3.79$  assuming  $n = 15$ . The strains have an inverse relation to the yield strength; the half-plate that has a higher strength will experience a lower strain at failure.



Figure 10. A simplified model of the CWP specimen subject to uniaxial loading

### 3.3 Interpretation of experimental measurements

As explained in [1], the “load versus stroke” plots were monitored during the tests and the tests were terminated as soon as it was judged that the maximum load was reached. Since these plots become very flat near the maximum load, it is difficult to determine whether the maximum load has actually been reached, especially given a small uncertainty in the load signal. An equivalent criterion to maximum load would be rapid increase in the CMOD as the crack propagates toward rupture, and so the behaviour

of the CMOD record was also checked. All but two of the tests (CWP-11 and CWP-16) were ended before complete rupture to avoid damage to the experiment equipment. The two tests indeed failed unexpectedly and motivated the monitoring of the CMOD versus stroke plots as part of the termination criteria. The post-processed test data show that the CMOD versus stroke curves did not reach a vertical asymptote in most of the tests, an example being CWP-09 shown in Figure 9. It is therefore reasonable to assume that the TSCs obtained from the experimental measurements are in fact conservative estimates.

The difference in the LVDT measurements above and below the weld raises the question, what should be taken as the TSC of the plate? As discussed in the following, it appears that a straightforward answer to this question is not readily available. Whereas in [2] the TSCs were taken to be the maximum of the strains measured above and below the flaw, in [4] the TSCs were taken to be the average of measured strains. In neither of these papers are the assumptions leading to these choices discussed. The difficulty stems from the fact that the experimental set-up actually leads to a constant stress in the plate rather than a constant strain; at constant stress, the strain differs in the plate sections above and below the flaw. This makes it difficult to estimate the “strain” capacity of the plate, a quantity that is intended to correspond to a strain-controlled process. It is worth emphasizing that the present work concerns prediction of the experimental failure strain. Deducing design recommendations from CWP measurements is not discussed here and may follow in a separate study.

In this work, the WM always overmatches the BM and so at a constant stress the strain is lower in the WM. Consider the case of the HAZ flaw location. The WM “shields” the flaw from strains in the plate on the opposite side of the weld from the flaw. It may be assumed that the flaw behaves as if it were located in a homogeneous plate with properties the same as those of the plate next to the flaw. This assumes that the strains in the vicinity of the flaw tip are determined by the plate properties, *i.e.*, that the material is symmetric about the flaw. It is doubtless true that the strain on the weld side of the flaw is lower than that in the plate, but the preceding assumption should work as a close approximation. Thus, for a flaw in the HAZ the TSC of the plate is taken to be the strain measured in the half-plate on the flaw side of the weld.

For WM flaws the situation is more complicated. In that case, the local properties in the flaw-tip region are different than those in remote regions. It is assumed that the flaw-tip deformations are controlled by the WM tensile properties. This assumes that the flaw behaves as if it were located in a plate of WM properties subject to the same nominal stress as in the original plate. For constant stresses, the strain in the BM half-plates on the two sides of the weld are different depending on whether the half-plate is weaker or stronger than average plate properties. The average of the two strains should give a value close to that expected for a plate of average tensile properties and is taken to be the TSC of the plate in the case of flaws in the WM.

## 4. RESULTS AND DISCUSSION

### 4.1 Treatment of inhomogeneities in prediction of the TSC

Consistent with the assumptions made in Section 3.3, in the case of HAZ flaws the  $J_D$  curves are calculated using the average tensile properties of the BM given in Table 4. For WM flaws,  $J_D$  is calculated using the average tensile properties of the weld metal (*i.e.*, assuming a uniform plate of WM properties). To account for the differences between the remote strains in the BM and WM, an equivalent plate is defined with BM properties in the remote regions and it is required that the plates be in equilibrium at equal nominal remote stresses. The (true) strain capacity in the equivalent plate  $\epsilon_{TSC}^{eq}$  may be obtained from equation (15) as

$$\varepsilon_{\text{TSC}}^{\text{eq}} = \frac{\sigma_y^{\text{BM}}}{E} \left( \frac{\sigma_y^{\text{WM}}}{\sigma_y^{\text{BM}}} \right)^{n^{\text{BM}}} \left( \frac{E \varepsilon_{\text{TSC}}}{\sigma_y^{\text{WM}}} \right)^{\frac{n^{\text{BM}}}{n^{\text{WM}}}} \quad (17)$$

where  $\varepsilon_{\text{TSC}}$  is the true TSC of a uniform plate with WM properties. Note that equation (17) is written in terms of true strains and appropriate conversions (true to engineering and vice versa) need to be applied when using this equation. TSC values are presented in terms of engineering strain in the present work.

As also pointed out previously, the actual flaw geometry inevitably differs somewhat from that of the ideal FEA flaw geometry, and  $J$  values for a semi-elliptical flaw are used. Flaw length and depth differ somewhat from target values, and  $J_R$  curves are obtained for each flaw depth by interpolating between values measured for different flaw depths (see Section 2, Table 1-Table 3). To account for experimental uncertainties in  $J_R$  curves, the TSCs are estimated by assuming a  $\pm 10\%$  variation in the coefficients  $c_1$  and  $c_2$  of the  $J_R$  curve in Table 1-Table 3. This provides an estimate of the error in predicted TSC resulting from uncertainties in the  $J_R$  curves.

#### 4.2 Predictions of TSC in CWP specimens

The ductile instability and initiation limit state methods presented in Section 2 were applied to each CWP test. For the ductile instability solution, the system of equations defined by (1) was solved numerically using a Newton-Raphson scheme. The solution is shown graphically for CWP-09 and CWP-11 as two representative examples in Figure 11. The predicted TSCs obtained are compared with the measured remote strains in Figure 12. For completeness, remote strains measured both below and above the flaw are shown by including vertical error bars; the average is also shown, notwithstanding the argument above concerning selection of the relevant strain. The horizontal error bars show the uncertainty in predicted TSC arising from the assumed  $\pm 10\%$  uncertainty in the  $J_R$  curves. The data corresponding to Figure 12 are included in Table 6. An interesting observation is that the slight uncertainties introduced (through variation of  $c_1$  and  $c_2$ ; see above) can lead to relatively large differences ( $\sim 25\%$  on average, and up to 60% in some cases *e.g.* CWP-27) in predicted TSC values.

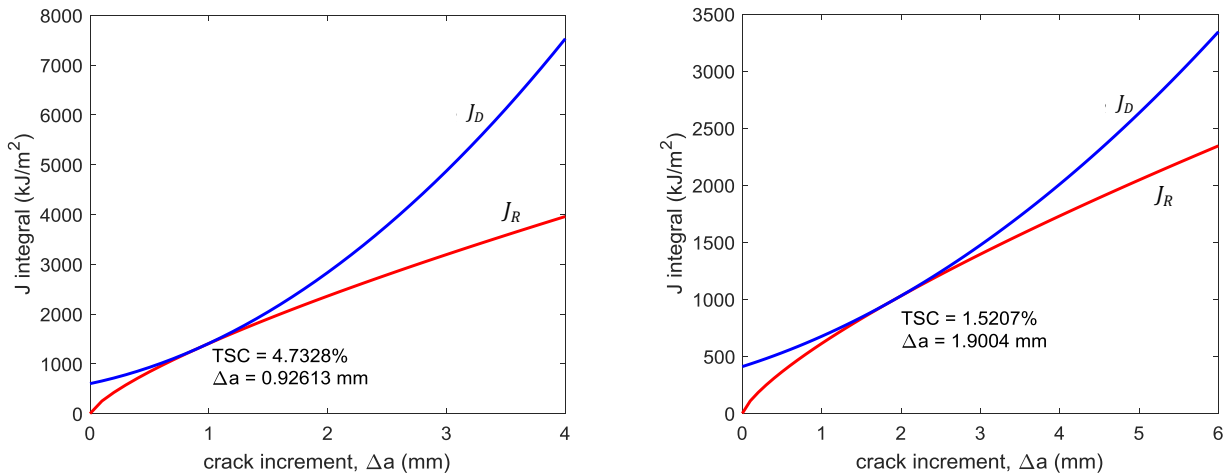


Figure 11. Ductile instability limit state solutions for a) CWP-09 and b) CWP-11. Note that only one  $J_D$  curve is shown in each case (*i.e.*, curves corresponding to variations in  $J_R$  values  $c_1$  and  $c_2$ , and to increasing strain, are not shown).

Figure 13 shows the predicted ductile instability limit strains without considering the variations in  $c_1$  and  $c_2$  versus the measured TSCs. For the HAZ tests, the TSC is the measured remote strain in the half-plate next to the flaw; for WM tests the TSC is the average of remote strain on both sides of the weld; see also Section 3.3.

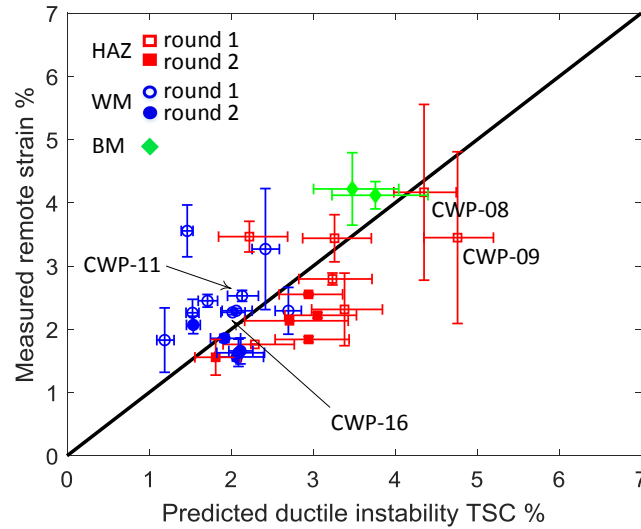


Figure 12. Measured remote strains versus predicted TSCs of CWP specimens

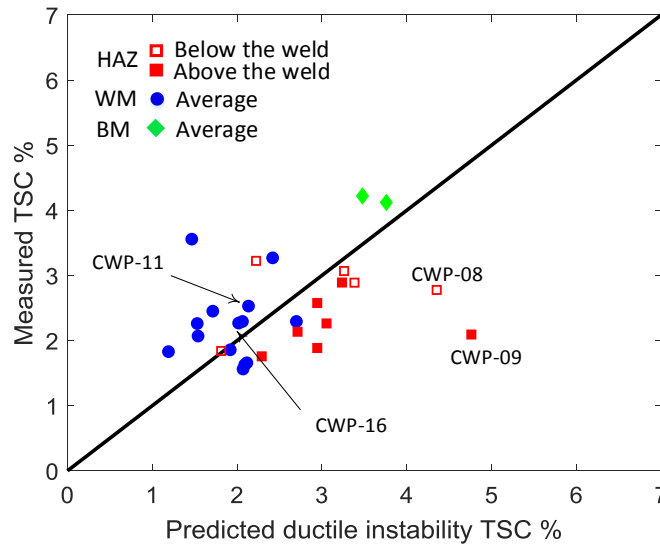


Figure 13. Measured versus predicted TSCs of CWP specimens. Variations of  $c_1$  and  $c_2$  are not considered in the numerical predictions. For HAZ flaws, the measured TSC is the remote strain in the half-plate next to the flaw; for WM and BM flaws the measured TSC is the average of remote strain on both sides of the weld.

The significance of the four tests CWP-08, CWP-09, CWP-11, and CWP-16 marked on Figure 12 and Figure 13 is as follows. The tests CWP-08 and CWP-09 have the largest discrepancy between maximum and minimum measured remote strains. On the other hand, in CWP-11 and CWP-16 the maximum and minimum measured strains are nearly equal (*i.e.*, nearly uniform strains were observed

in these plates). The CMOD versus applied strain and load versus applied strain of these two groups of tests are shown in Figure 14 and Figure 15. These two groups appear to identify two extreme conditions in CWP specimens. In the first group, namely, CWP-08 and CWP-09, the half-plates must have had significantly different tensile properties leading to different strains above and below the flaw. This seems to have in turn led to premature termination of the test given that the CMOD curves have not reached their vertical asymptotes at termination in spite of the fact that load versus applied strain curve has become nearly flat. This aligns well with the observation that the predicted TSCs are relatively larger than the measured TSCs for these two test as can be seen in Figure 13. In contrast, the CMOD curves corresponding to the second group of tests (CWP-11 and CWP-16, the tests with unexpected failure) have reached an asymptotic region at termination, clearly marking the plate's strain capacity. The predicted and measured TSCs are in excellent agreement in these two tests. This is also the case for the BM-only tests where the plate inhomogeneity is presumably minimized.

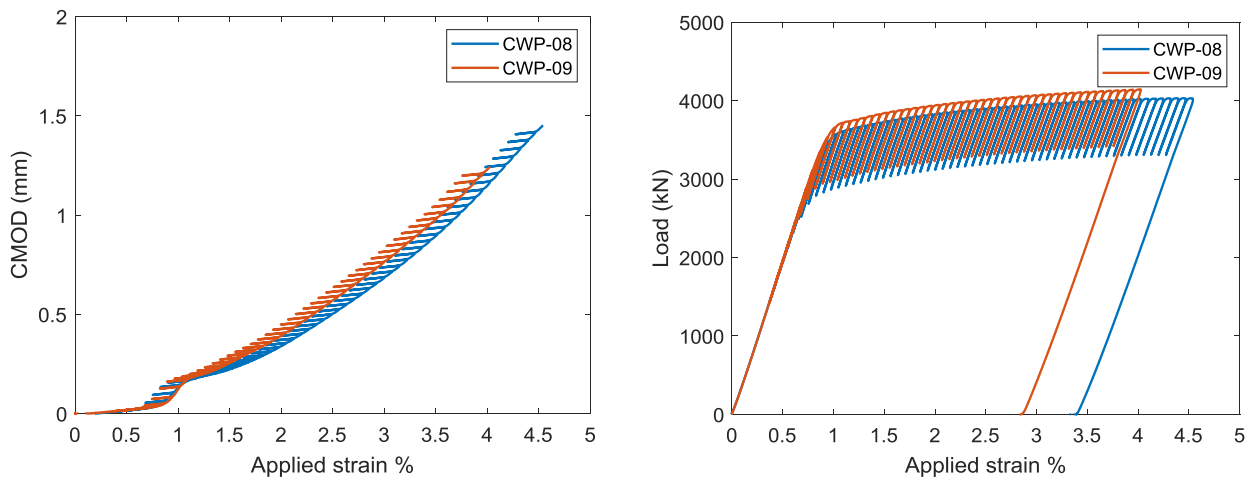


Figure 14. a) CMOD versus applied strain and b) load versus applied strain for CWP-08 and CWP-09

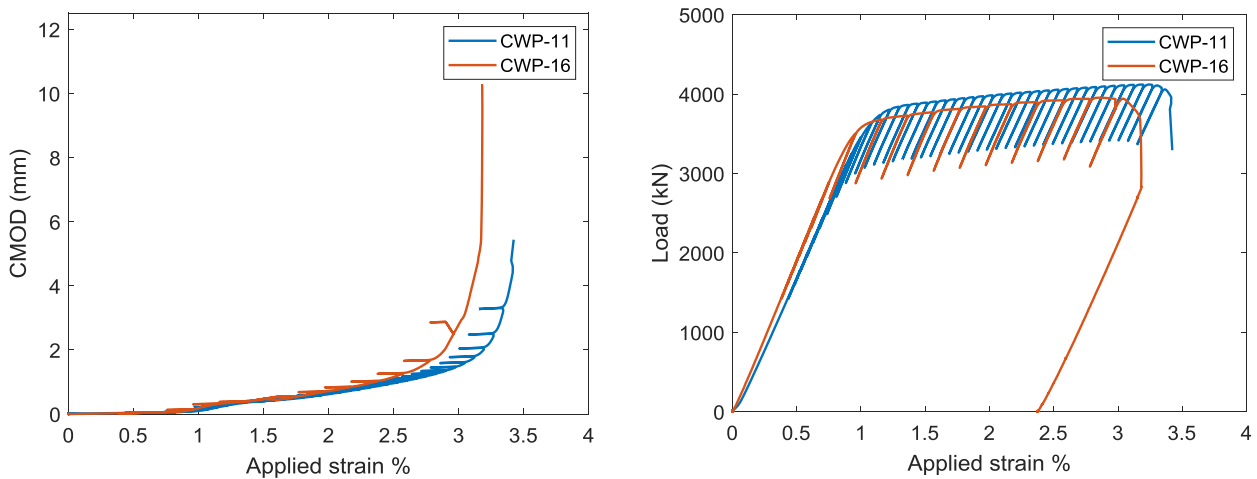


Figure 15. a) CMOD versus applied strain and b) load versus applied strain for CWP-11 and CWP-16

The scatter in Figure 12 and Figure 13 may be attributed to the inevitable and non-quantified scatter in various test conditions including the tensile properties of the X100 steel used in making CWP and SE(T) specimens, variations in flaw shape, and premature termination of the tests (see Section 3.2). A similar type of behaviour has been reported in [5, Figures 19 and 20] for CTOD-based ductile instability limit state solutions using values of CTOD obtained from  $J_R$  curves measured in SE(T) tests.

To determine which of the two approaches ( $J$ -based or CTOD-based) gives a better representation of experimental TSCs, a “normalized error”  $n_E$  is calculated between the measured and predicted TSC data points in Figure 13 and in Table 9 of [4] as

$$n_E = \frac{\sqrt{\sum(\text{TSC}_{\text{pred}} - \text{TSC}_{\text{meas}})^2}}{\sqrt{\sum(\text{TSC}_{\text{meas}})^2}}.$$

This definition of error gives a measure of the agreement between the predictions and measurements; the better the agreement, the smaller the error. Excluding CWP-08 and CWP-09 which were identified as outliers as well as the tests for which experimental data were not available in the present study, the normalized error is 0.23 for the present  $J$ -based approach and 0.36 for the CTOD-based approach. Hence, it is concluded that ductile instability TSCs deduced from  $J$  is more predictive than those deduced from CTOD.

Next, the TSCs obtained using the initiation limit state method are presented. The choice of the initiation crack growth  $\Delta a_{\text{init}}$  has a significant impact. Results using  $\Delta a_{\text{init}}=0.2$  mm and  $\Delta a_{\text{init}}=0.5$  mm are shown in Figure 16 and Figure 17, respectively. For completeness, the average and range of measured remote strains are used in these figures (as in Figure 12).

From Figure 16, it is observed that initiation strains using  $\Delta a_{\text{init}}=0.2$  mm are smaller than measured remote strains at failure (Figure 16a) and predicted instability strains (Figure 16b). This is as expected, because the  $J_R$  curves demonstrate that there is significant increase in toughness beyond a crack growth of 0.2 mm. With  $\Delta a_{\text{init}}=0.2$  mm, the crack growth associated with initiation is limited to a maximum of approximately 10% of the initial flaw depth and the predicted initiation strains are conservatively lower than both measured remote strains and predicted ductile instability strains. The initiation limit state solutions are nearly insensitive to uncertainties in the resistance curves so that the horizontal error bars in Figure 16 and Figure 17 are negligible in most cases.

However, it is observed in Figure 17 that considering initiation to occur at  $\Delta a_{\text{init}}=0.5$  mm (which has been suggested in [4,24]) yields initiation strain predictions that are in many cases larger than the measured maximum strain capacities or even the predicted ductile instability limit state strains. Thus,  $\Delta a_{\text{init}}=0.5$  mm appears to be too large to conservatively characterize initiation of crack growth for the flaw depths ranging between approximately 2 to 6 mm analyzed here.

The present re-analysis of available CWP data demonstrates that  $J$ -integral can be usefully calculated beyond “validity” limits and allows CWP tensile strain limits to be estimated with reasonable accuracy. Sources of uncertainty are limitations in experimental control, inherent scatter in  $J_R$  measurement in SE(T) specimens, and  $J_D$  calculation for CWP specimens. Application of the present methodology to pipelines requires further analysis for pipe geometries to obtain robust driving-force estimates and investigate the practical mythology to predict instability strains. This requires further effort and may be the subject of a separate study. Nonetheless, strain based design using  $J$ -integral is thus validated, supporting first-principles estimation of initiation and instability using only small-scale SE(T) data and  $J$ -integral calculations for CWP.

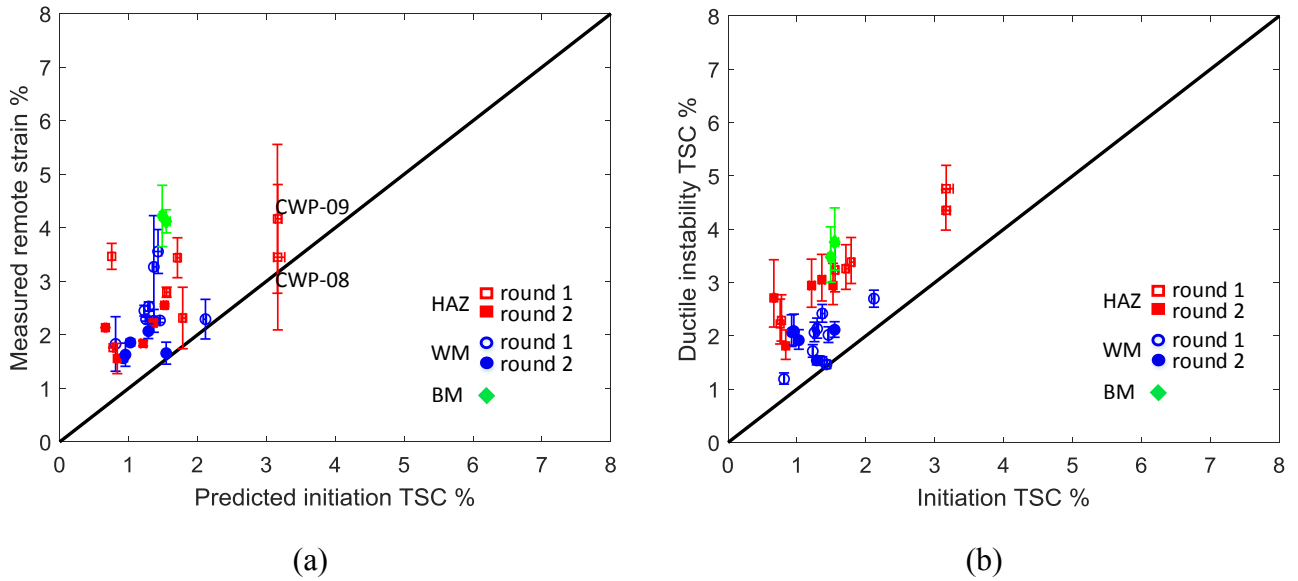


Figure 16. Comparison of predicted initiation limit state strains (abscissa) using  $\Delta a_{init}=0.2$  mm with a) measured remote strains, and b) predicted ductile instability limit state strains.

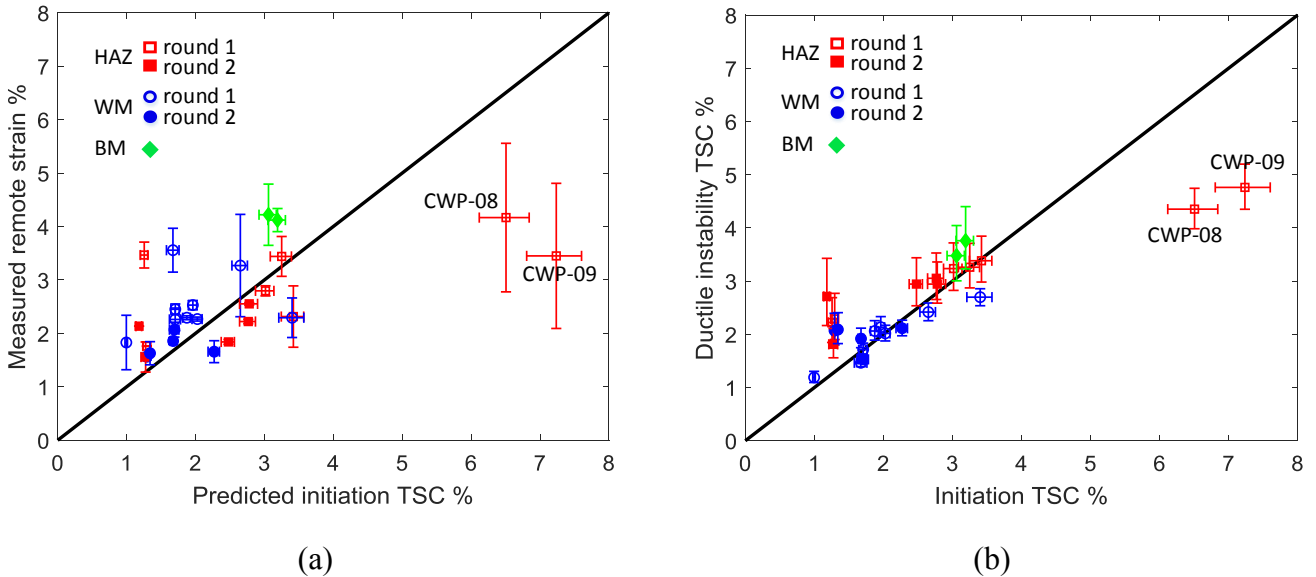


Figure 17. Comparison of predicted initiation limit state strains (abscissa) using  $\Delta a_{init}=0.5$  mm with a) measured remote strains, and b) predicted ductile instability limit state strains.

### 4.3 Applicability of Charpy toughness in predictions of TSC

Measured remote strains are compared with initiation limit state predictions from CTOD in Figure 18 [4]. The following assumptions were made in [4]: CTOD was used as the driving force; CTOD toughness data were extracted from Charpy tests; and the initiation crack growth was taken to be  $\Delta a_{init}=0.5$  mm. It was concluded in [4] that the predictions obtained based upon these assumptions are closer to the measured remote strains than the predictions obtained using SE(T) toughness data (for both initiation and ductile instability solution methods). As pointed out in the Introduction, one of the

objectives of this work has been to assess this arguably surprising conclusion. To shed more light on this topic, the literature was interrogated to examine the state of the art in estimating  $J_R$  curves from CVN data. Fortunately, Wallin has reviewed this question in a recent paper [25]. An earlier paper by Schindler [26] also includes an equation to estimate  $J_R$  curves. The estimation equations according to Wallin are

$$J_R^{\text{Wallin}}(\Delta a) = J_{1\text{mm}} \Delta a^m \quad (18)$$

where

$$J_{1\text{mm}} = 296 \left( \frac{\text{CVN}}{100} \right)^{1.28}, \quad (19)$$

$$m \approx \left( \frac{J_{1\text{mm}}}{12517} \right)^{0.2},$$

where CVN is the upper-shelf Charpy energy in Joules,  $\Delta a$  is in mm, and  $J_R$  is in  $\text{kJ/m}^2$ . With the resistance curves in this paper fitted to the form  $J_R = c_1 \Delta a^{c_2}$ , it is evident that  $m$  is identical to  $c_2$  and  $c_1$  is the value of  $J$  at 1 mm crack growth, *i.e.*,  $J_{1\text{mm}}$  in Wallin's terminology. That is,  $c_1 = J_{1\text{mm}}$  and  $c_2 = m$  in Wallin's approximation. The estimation equation according to Schindler is

$$J_R^{\text{Schindler}}(\Delta a) = 11.44 \text{ CVN } \varepsilon_u^{1/3} \Delta a^{2/3}, \quad (20)$$

where  $\varepsilon_u$  is the strain at ultimate stress (*i.e.*, uEl). That is,  $c_1 = 11.44 \text{ CVN } \varepsilon_u$  and  $c_2 = 2/3$  in Schindler's approximation.

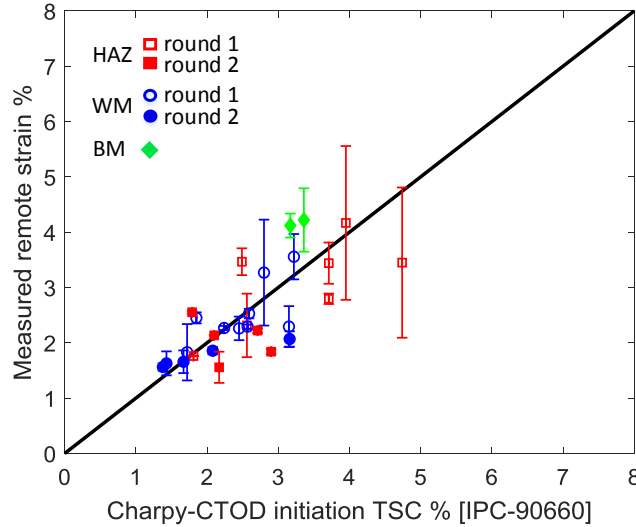


Figure 18. Comparison of measured remote strains with initiation limit state strains reported in [4] based on CTOD and Charpy toughness.

The values of  $c_1$  and  $c_2$  estimated from these equations are compared in Table 7 for different flaw locations and weld rounds with the corresponding values measured using SE(T) specimens with cracks of initial size 6 mm at temperature  $T = 25^\circ\text{C}$ . The Charpy impact energies given in the Table were taken from [13]. It is evident that the  $J_R$  curve parameters estimated from CVN values fit the values measured by SE(T) tests reasonably well. The  $c_1$  values are in the proper range, with Wallin's values

being somewhat conservative and Schindler's being somewhat unconservative; the  $m$  values are in reasonable accord with SE(T) results. It must be borne in mind that the  $J_R$  curves measured in the present work are geometry-dependent, *i.e.*, they are not strictly "valid" and vary with the size of the flaw and the ligament. In other words, constraint varies with the specimen geometry and loading mode, and corresponding  $J_R$  curves vary accordingly. Care has been taken to match constraints between SE(T) specimens and CWP specimens as closely as possible. While the conversion schemes discussed here provide reasonably accurate estimations of  $J_R$ , they may not perform so well in other applications.

It is concluded from the above that it is possible to make reasonable estimates of  $J_R$  in the upper shelf from CVN data. However, estimating toughness curves (either CTOD or  $J$ ) from Charpy tests requires empirical correlations and conversions as shown above, which can in turn impact accuracy of the numerical predictions in many cases.  $J$ -based calculations allow adoption of standard fracture mechanics tests for accurate predictions of strain capacities without need to empirical conversions and avoid the controversy over the definition of CTOD as well.

Table 7. Comparison of  $J_R$  coefficients obtained from different conversions with SE(T) results.  $J$  values are given in  $kJ/m^2$ .

		Wallin		Schindler		CANMET 6 mm crack			
		$\epsilon_u$ %	CVN (J)	$c_1 \equiv J_{1mm}$	$c_2 \equiv m$	$c_1 \equiv J_{1mm}$	$c_2$	$c_1 \equiv J_{1mm}$	$c_2 \equiv m$
	BM	4.9	300	1098	0.615	1256	0.667	1164	0.62
WM	Round 1	7.4	205	674	0.558	985	0.667	564	0.71
	Round 2	7.4	160	491	0.523	768	0.667	647	0.784
HAZ	Round 1	7.4	237	812	0.579	1138	0.667	1132	0.56
	Round 2	4.9	250	869	0.587	1047	0.667	948	0.604

## 5. CONCLUSIONS

In this work,  $J$ -based predictions of TSC based on ductile instability and initiation limit states have been compared with values measured in CWP tests. The following conclusions are made:

1. Predictions of TSC based on ductile instability using  $J$  resistance curves compare well with TSC values measured on curved wide plates. The agreement is significantly better than that obtained using CTOD. The normalized error in the measured TSCs with respect to the predicted TSCs is 0.23 for the  $J$ -based results whereas it is 0.36 for the CTOD-based results reported in [4].
2. Predicted TSC values based on initiation crack growth of 0.2 mm give conservative estimates of measured TSC. Using growth of 0.5 mm as initiation criterion was found to be unconservative in many cases.
3. The ductile instability limit state solutions can be highly sensitive to the uncertainties in  $J$  driving and resistance curves. For a 10% variation in the coefficients of the  $J_R$  curve, predictions of the ductile instability limit state solutions can vary by 25% on average. In contrast, initiation limit state strains are nearly insensitive to these variations.
4. The scatter in the predicted versus measured strain capacities stems mainly from the variation of the tensile properties of the X100 steel. A slight difference in the yield strength can lead to a large variation in the strain owing to the flatness of the stress-strain curve.
5. The post-processed raw test data of CWP experiments showed that the remote strains measured above and below the flaw differ by ~50% on average. Because the tensile properties of a pipeline

vary along its length and circumference, and since most CWP tests were interrupted before final failure, the TSC values also vary and judgment is needed in choosing a value for design.

## ACKNOWLEDGEMENTS

This work has been funded by the Canadian Federal Program on Energy Research and Development (PERD) on fracture control of pipelines. The authors gratefully acknowledge Mark Gesing for the preparation of CWP models in ABAQUS and Jim Gianetto and Dong-Yeob Park for discussion and provision of the DOT-PRCI project references.

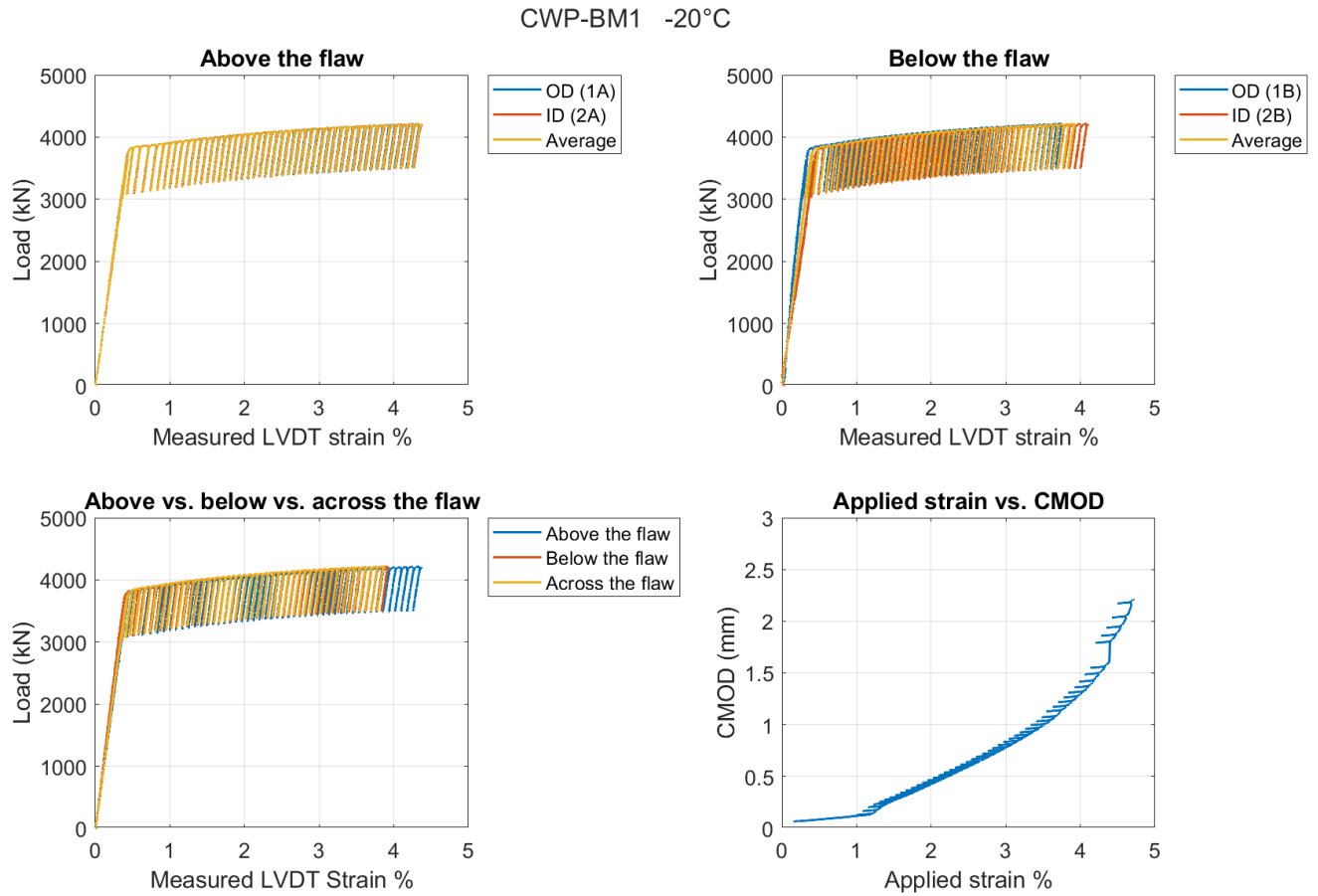
## REFERENCES

- [1] T. Weeks, J.D. McColskey, M. Richards, Weld Design, Testing, and Assessment Procedures for High-strength Pipelines Curved Wide Plate Tests, DOT Agreement DTPH56-07-T-000005, Final report 277-T-09, September, 2011 (<http://primis.phmsa.dot.gov/matrix/FilGet.rdm?fil=7333>)
- [2] Y.Y. Wang, H. Zhou, W.R. Tyson, J.A. Gianetto, M.A. Quintana, T.S. Weeks, Curved Wide Plate Test Results and Transferability of Test Specimens, DOT Agreement DTPH56-07-T-000005, Topical Report 277-T-11, January 21, 2012 (<http://primis.phmsa.dot.gov/matrix/FilGet.rdm?fil=7335>)
- [3] API Specification 5L, 2012, Specification for Line Pipe, 45th ed., American Petroleum Institute (API), Washington, DC.
- [4] Y.-Y. Wang, M. Liu, F. Zhang, D. Horsley, S. Nanney, Multi-Tier Tensile Strain Models for Strain-Based Design: Part 1—Fundamental Basis, Proc. 9th International Pipeline Conference (IPC2012), September 24-28, 2012, Calgary, Alberta, Canada, ASME, IPC2012-90690.
- [5] M. Liu, Y.-Y. Wang, Y. Song, D. Horsley, S. Nanney, Multi-Tier Tensile Strain Models for Strain-Based Design: Part 2—Development and Formulation of Tensile Strain Capacity Models, in: Int. Pipeline Conf., American Society of Mechanical Engineers, 2012: pp. 415–425.
- [6] M. Liu, Y.-Y. Wang, D. Horsley, S. Nanney, Multi-Tier Tensile Strain Models for Strain-Based Design: Part 3—Model Evaluation Against Experimental Data, in: Int. Pipeline Conf., American Society of Mechanical Engineers, 2012: pp. 427–438.
- [7] Park, Dong-Yeob, and James A. Gianetto, Review of Tensile Strain Capacity Prediction Models for Strain-Based Design of Pipelines. ASME Press. Vessel. Pip. Conf., 2019, vol. 58981.
- [8] M. Liu, Y.-Y. Wang, X. Long, Enhanced Apparent Toughness Approach to Tensile Strain Design, (2010) 187–194. doi:10.1115/IPC2010-31386.
- [9] G. Shen, R. Bouchard, J.A. Gianetto, W.R. Tyson, Fracture toughness evaluation of high strength steel pipe, in: ASME Press. Vessel. Pip. Conf., 2008: pp. 1275–1282.
- [10] D.Y. Park, W.R. Tyson, J.A. Gianetto, G. Shen, R.S. Eagleson, E. Lucon, T.S. Weeks, Small Scale Low Constraint Fracture Toughness Test Results, DOT Agreement DTPH56-07-T-000005, Final Report 277-T-06, September 2011 (<http://primis.phmsa.dot.gov/matrix/FilGet.rdm?fil=7330>).
- [11] G. Shen, J.A. Gianetto, W.R. Tyson, Development of procedure for low-constraint toughness testing using a single-specimen technique, CANMT-MTL report, MTL2008-18(TR), November 2008.
- [12] F. Zhang, H. Zhou, Y.-Y. Wang, M. Liu, Y. Song, Determination of J Resistance Curves From CWP Specimens, in: Int. Pipeline Conf., American Society of Mechanical Engineers, 2012: pp. 383–390.

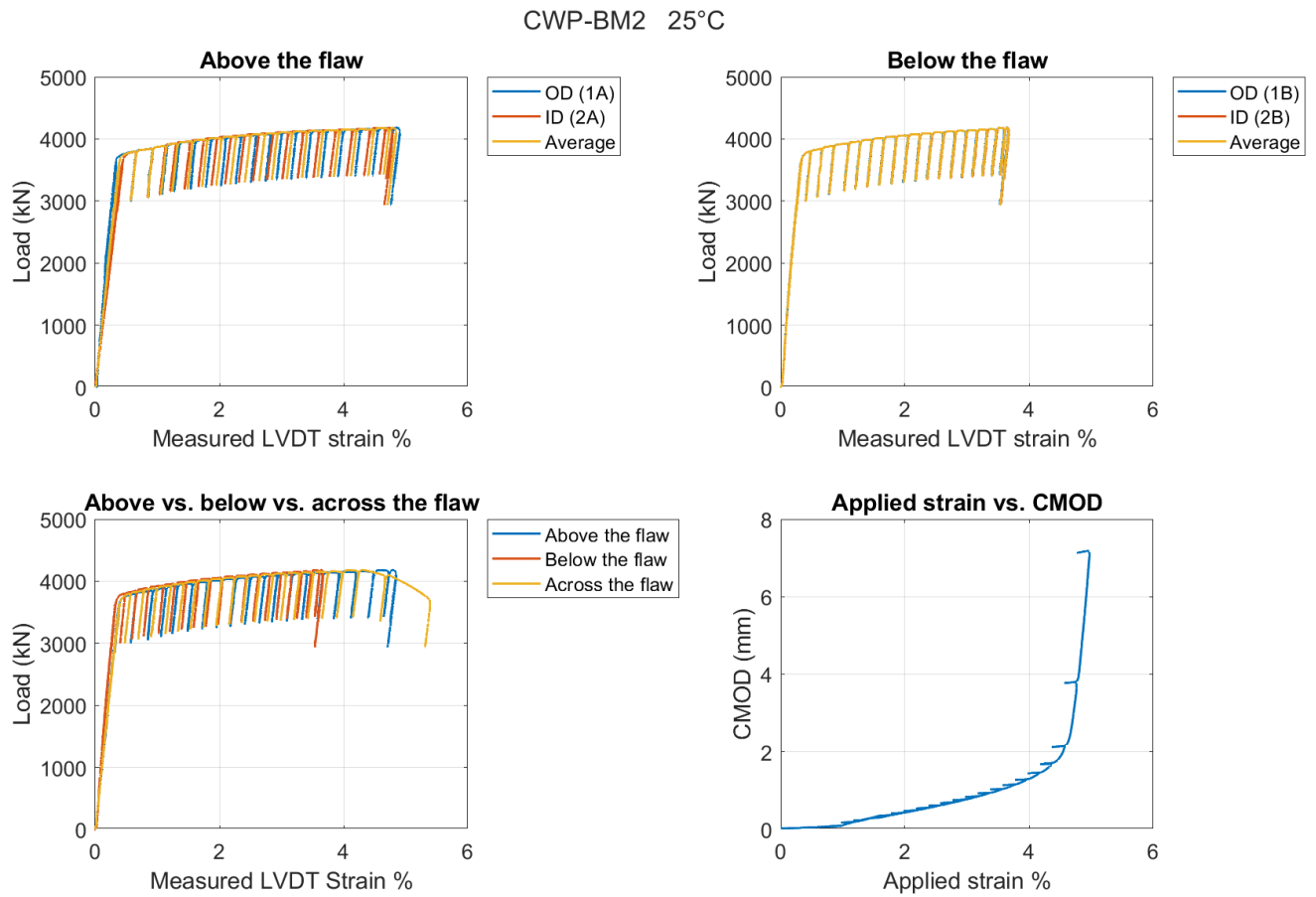
- [13] J.A. Gianetto, W.R. Tyson, D.Y. Park, G. Shen, E. Lucon, T.S. Weeks, M.A. Quintana, V.B. Rajan, Y.Y. Wang, Small Scale Tensile, Charpy V-Notch, and Fracture Toughness Tests, DOT Agreement DTPH56-07-T-000005, Final Report 277-T-05, September 2011 (<http://primis.phmsa.dot.gov/matrix/FilGet.rdm?fil=7329>).
- [14] S. Xu, W.R. Tyson, Effects of strain rate on strength, and of orientation on toughness, of modern high-strength pipe steels., *J. Pipeline Eng.* 14 (2015).
- [15] S. Xu, R. Bouchard, W.R. Tyson, Constitutive equation for structural steels, *Metall. Mater. Trans. A.* 35 (2004) 1410–1414.
- [16] W. Brocks, I. Scheider, Numerical aspects of the path-dependence of the  $J$ -integral in incremental plasticity, *GKSS Forschungszentrum, Geesthacht.* 1 (2001) 1–33.
- [17] American Society for Testing and Materials, ASTM E1820: standard test method for measurement of fracture toughness, (2015).
- [18] T.L. Anderson, Development of a Modern Assessment Method for Longitudinal Seam Weld Cracks. Pipeline Research Council Inc., Catalog No. PR-460-134401. 2016;95.
- [19] T.L. Anderson, *Fracture Mechanics: Fundamentals and Applications*, CRC press, 2017.
- [20] M. Smith, *ABAQUS/Standard User's Manual, Version 6.9*, Dassault Systèmes Simulia Corp, United States, 2009.
- [21] A. Pépin, T. Tkaczyk, N. O'Dowd, K. Nikbin, Limit Load Solution and Crack Driving Force Estimation Scheme for Embedded Flaws in Pipeline Girth Welds, in: *ASME 2015 Press. Vessel. Pip. Conf.*, American Society of Mechanical Engineers Digital Collection, 2015.
- [22] H. Lee, Estimation of Crack Driving Forces on Strength-mismatched Bimaterial Interfaces, *Nucl. Eng. Des.* 212 (2002) 155–164.
- [23] N. Nourpanah, F. Taheri, Development of a Reference Strain Approach for Assessment of Fracture Response of Reeled Pipelines, *Eng. Fract. Mech.* 77 (2010) 2337–2353.
- [24] Y.-Y. Wang, M. Liu and Y. Song, Second Generation Models for Strain-Based Design, PRCI Project ABD-1, US DOT Agreement DTPH56-06-T000014, Final Report, August 30, 2011.
- [25] K. Wallin, A Simple Fracture Mechanics Based Charpy-V Impact Energy Criterion for Plastic Collapse, *Eng. Fract. Mech.* 237 (2020) 107247.
- [26] H. Schindler, The Correlation between Charpy Fracture Energy and Fracture Toughness from a Theoretical Point of View, *Proc. 12th Eur. Conf. Fract. (ECF 12)*, EMAS, Sheffield, 1998: pp. 841–846.

## APPENDIX A. EXPERIMENTAL MEASUREMENTS OF CWP TESTS

The experimental measurements corresponding to the tests summarized in Table 6 are given below.

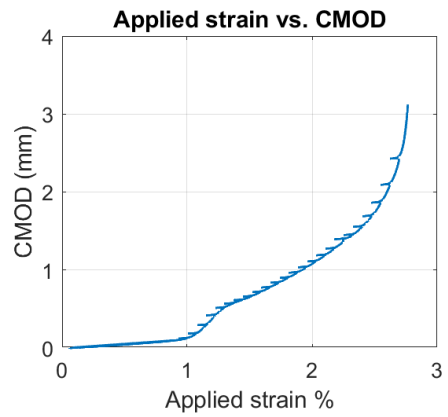
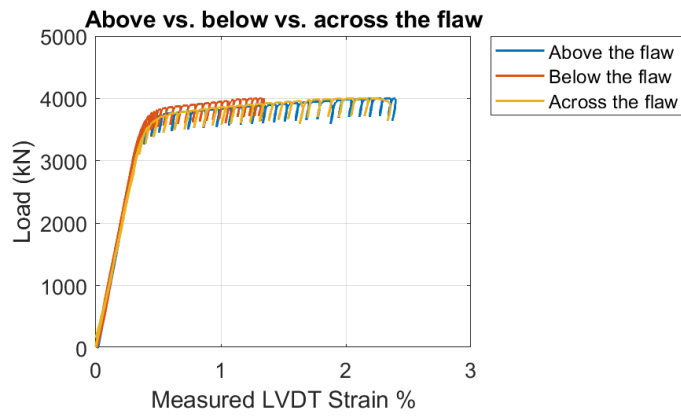
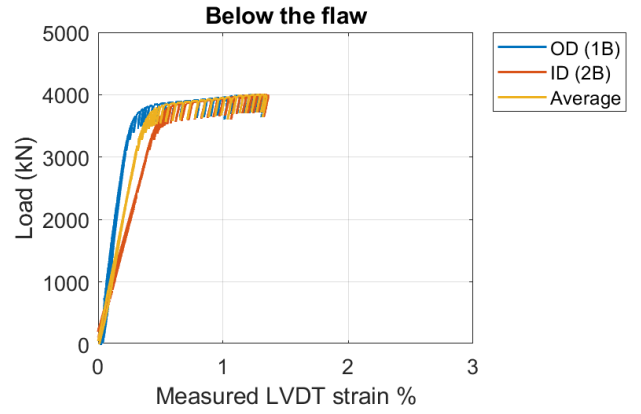
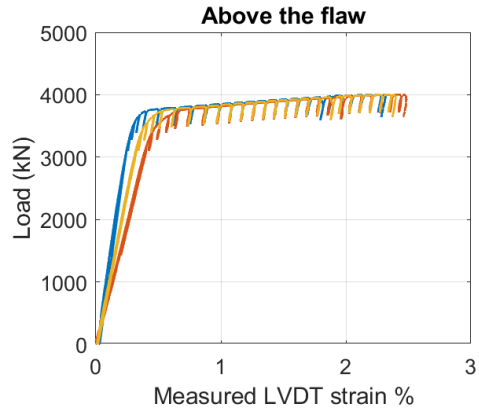


Note: Only the ID measurement was available above the flaw in CWP-BM1. The OD strain was taken to be equal to the ID strain.

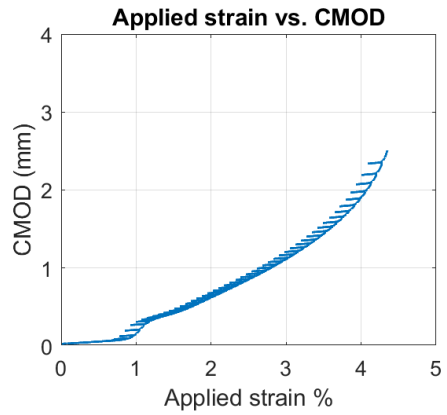
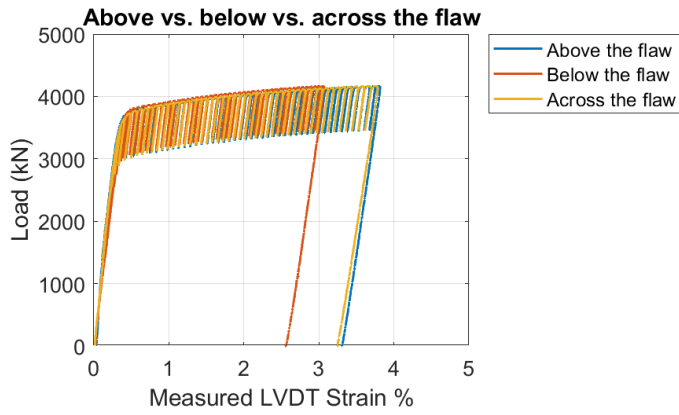
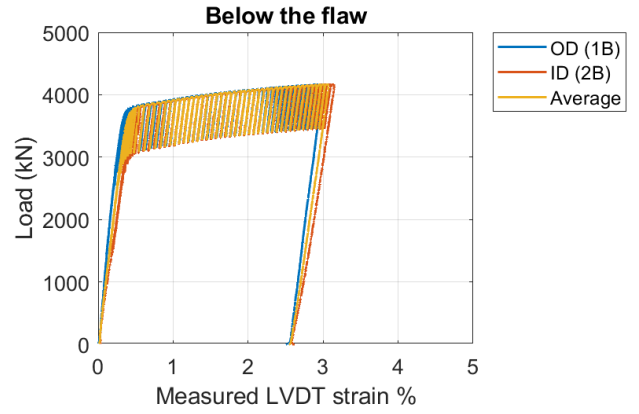
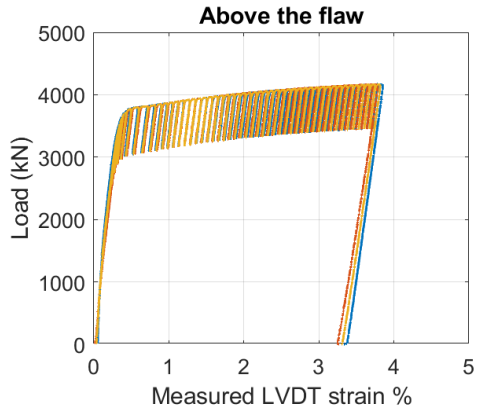


Note: Only the OD measurement was available below the flaw in CWP-BM2. The ID strain was taken to be equal to the OD strain.

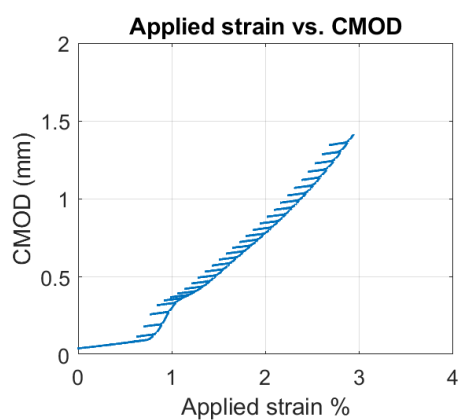
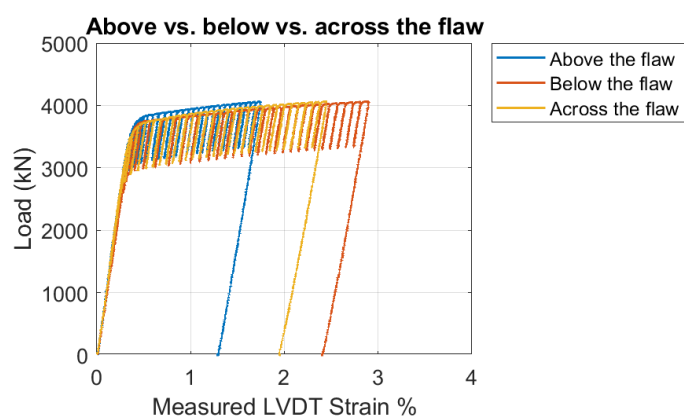
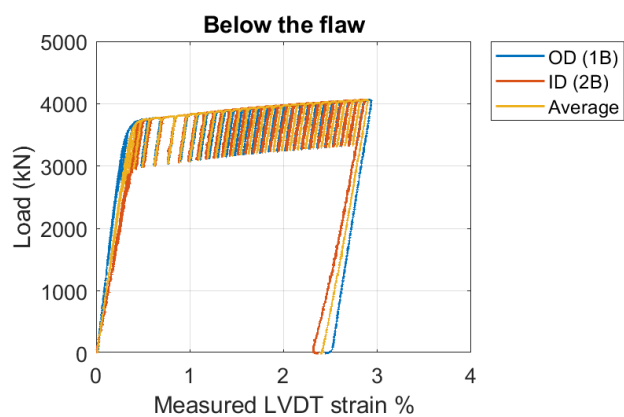
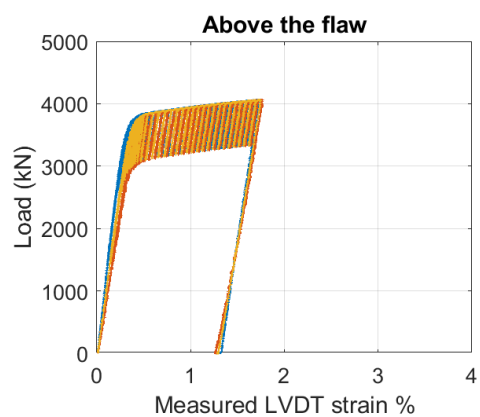
CWP-1 WELD 25°C



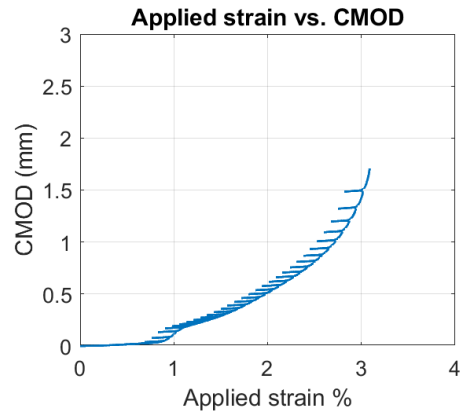
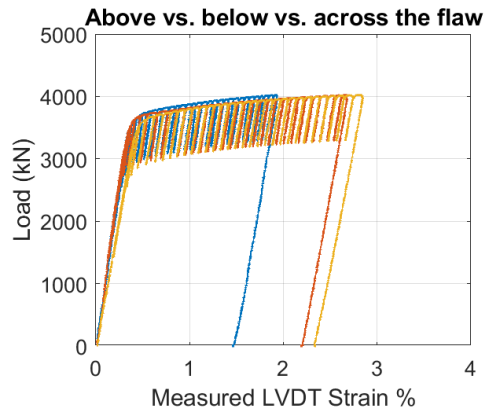
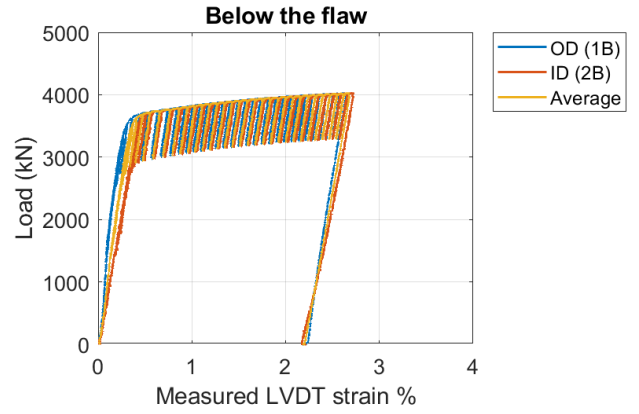
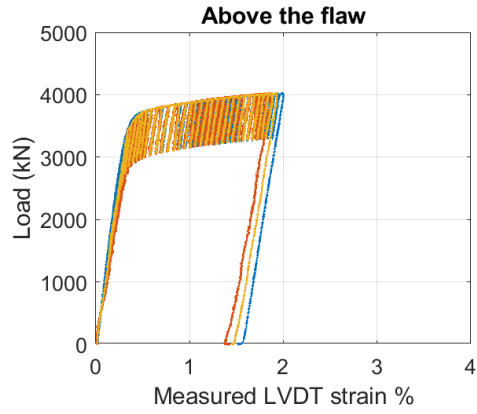
CWP-2 HAZ -20°C



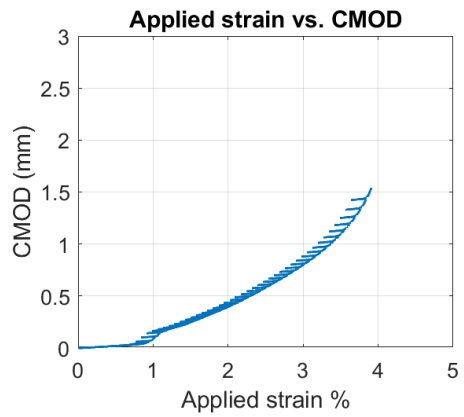
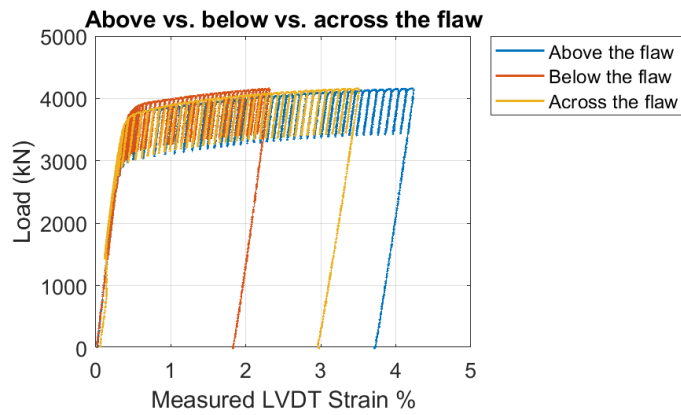
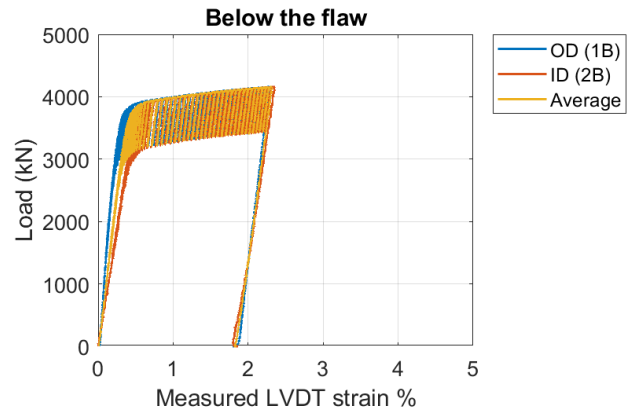
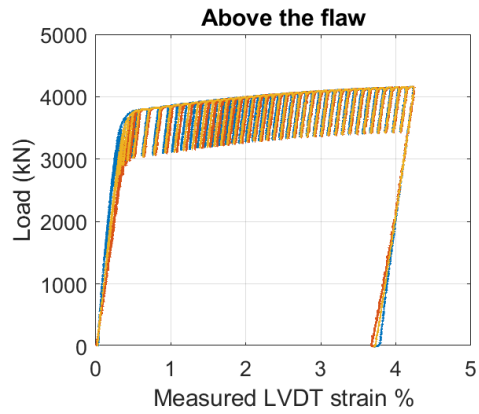
## CWP-5 HAZ -20°C



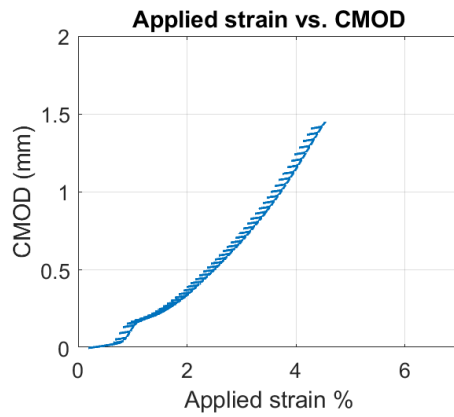
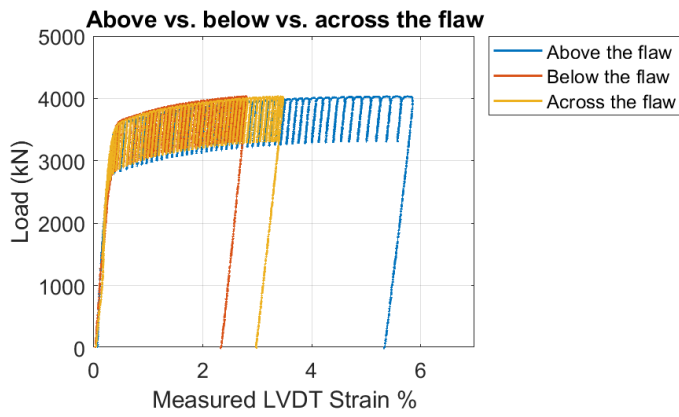
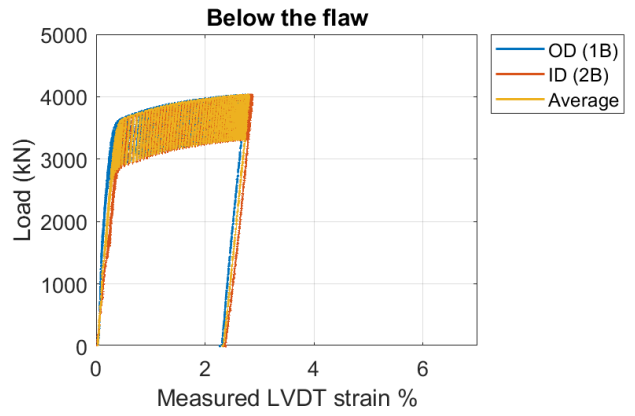
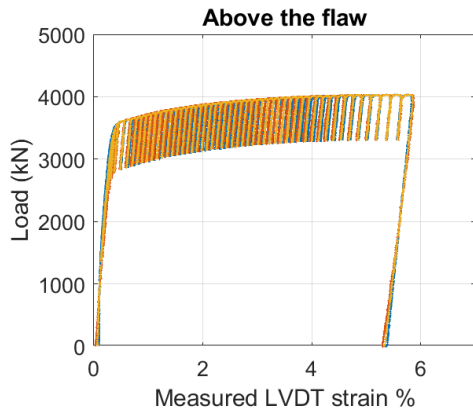
CWP-6 WELD 25°C



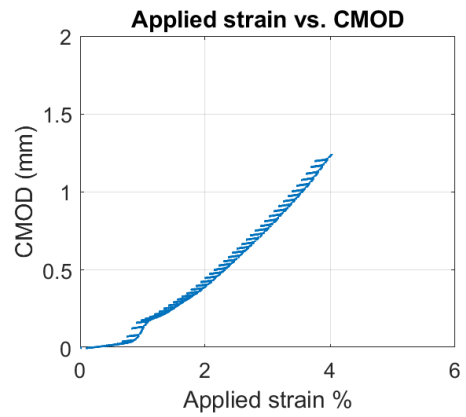
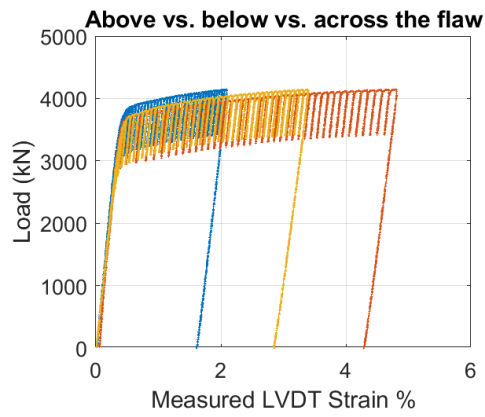
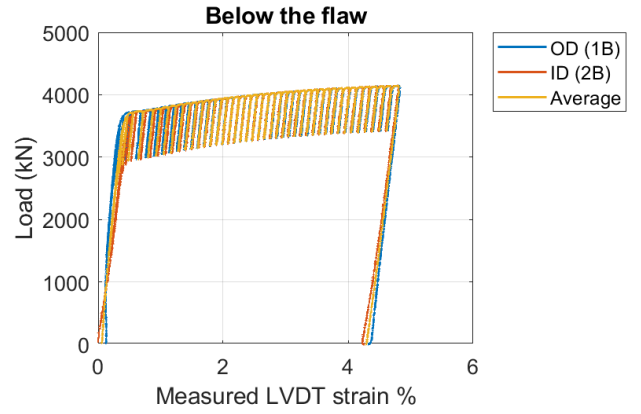
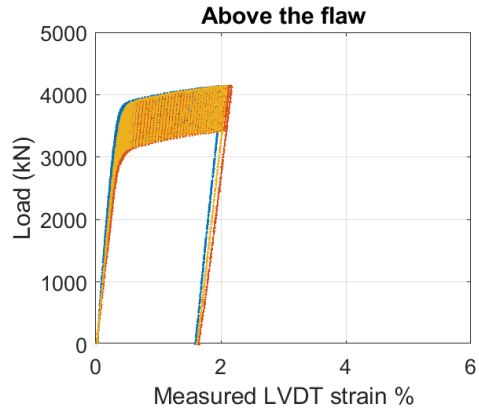
CWP-7 HAZ -20°C



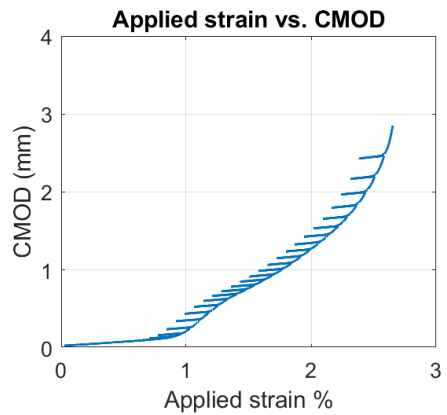
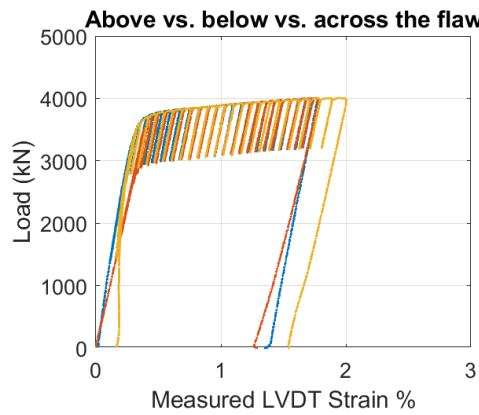
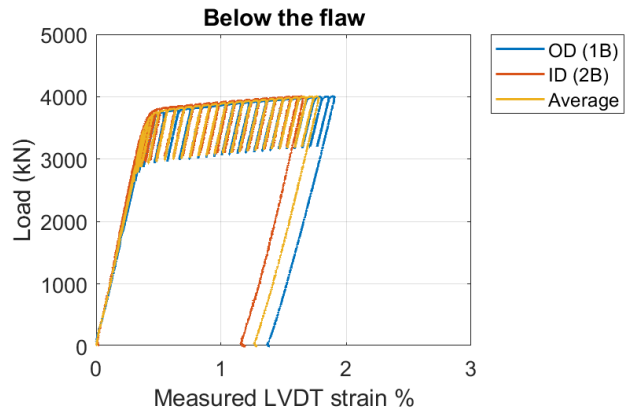
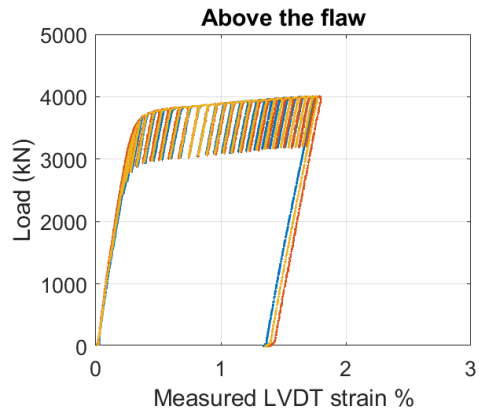
CWP-8 HAZ 25°C



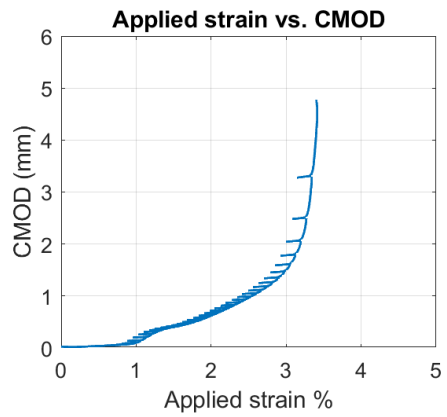
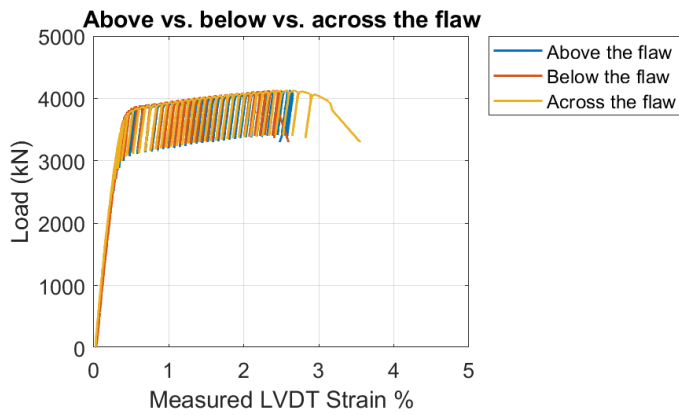
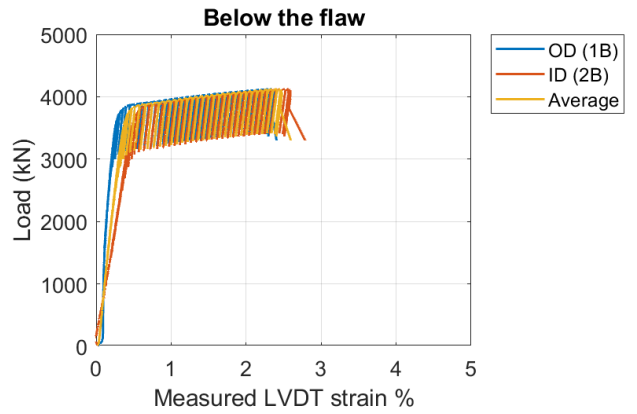
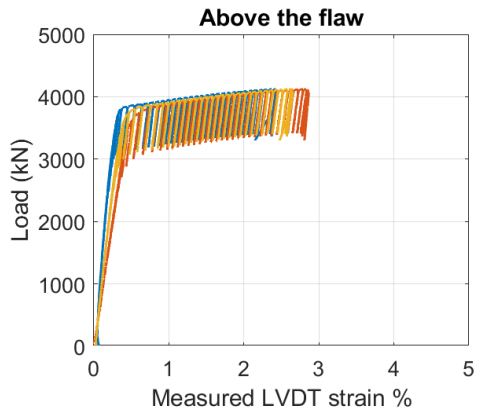
CWP-9 HAZ -20°C



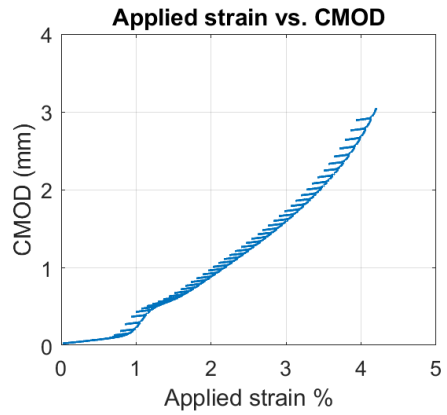
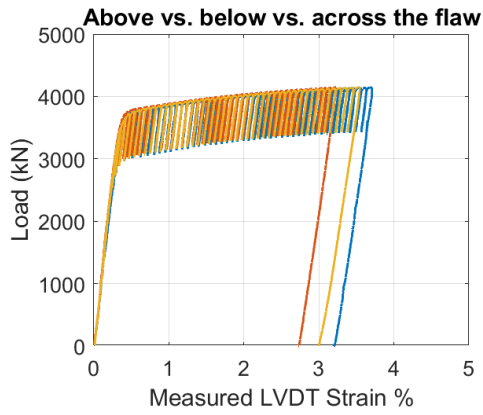
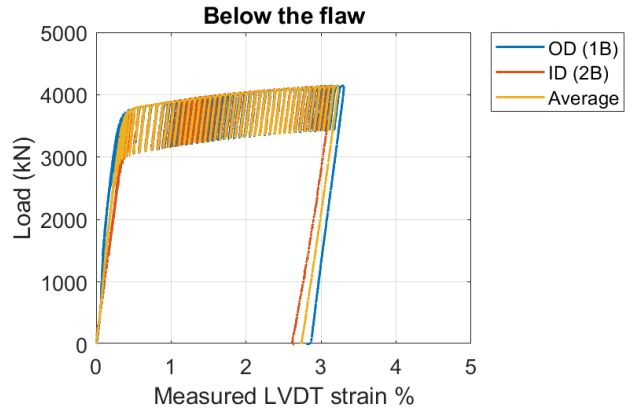
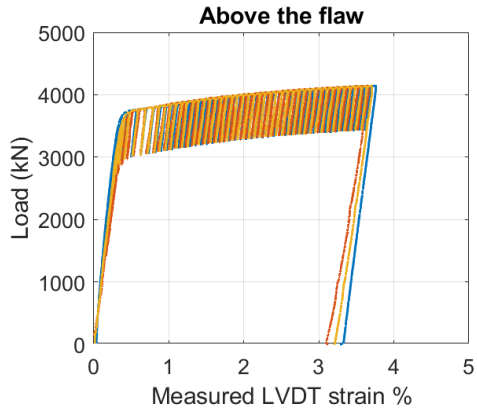
CWP-10 Weld -20°C



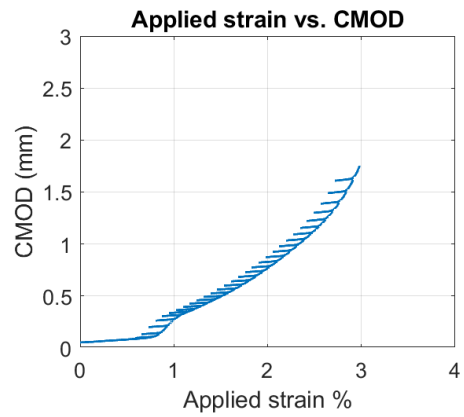
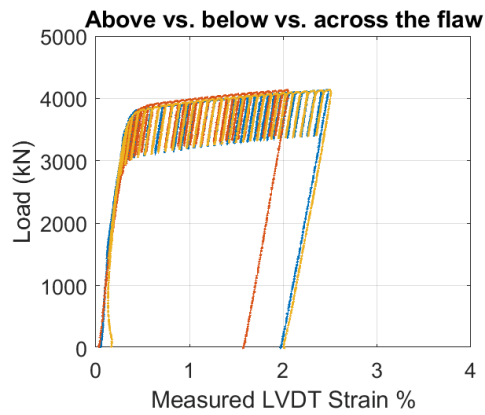
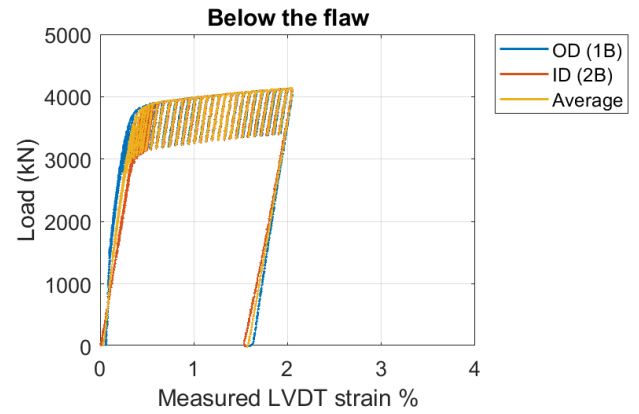
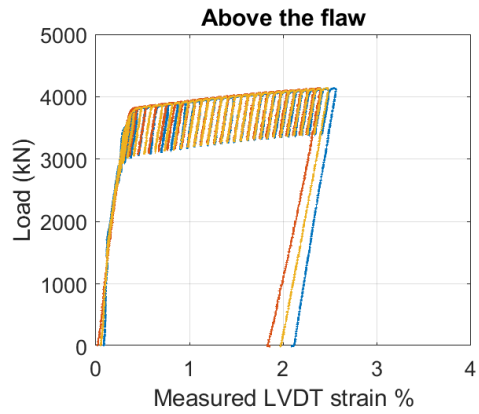
CWP-11 Weld -20°C



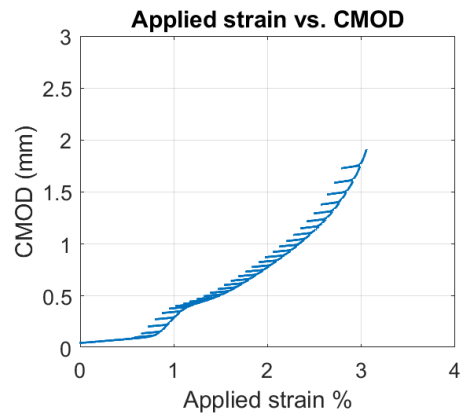
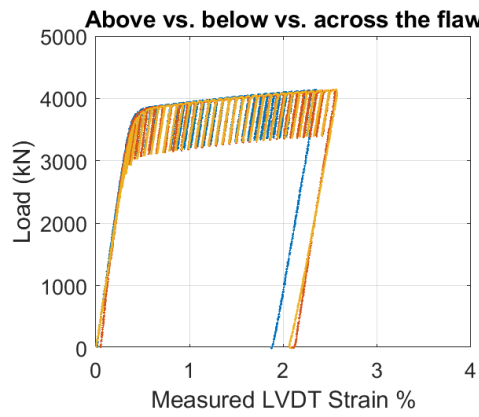
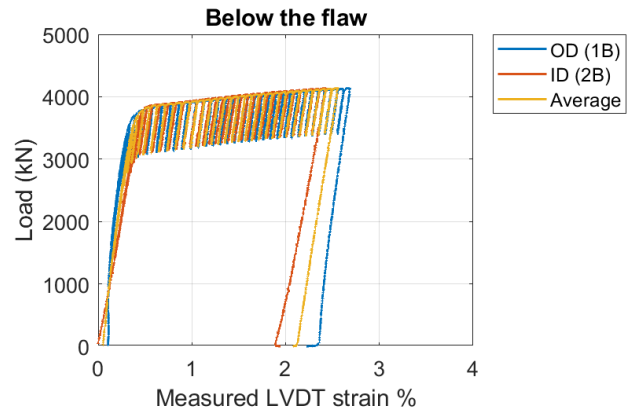
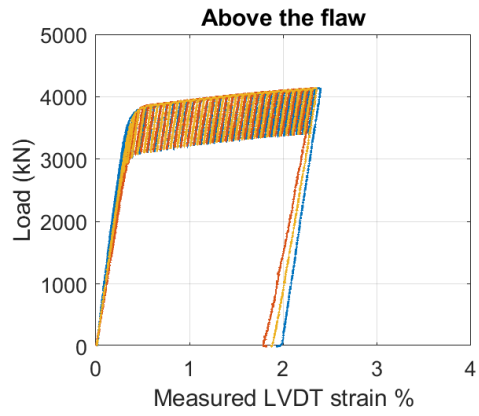
CWP-12 HAZ -20°C



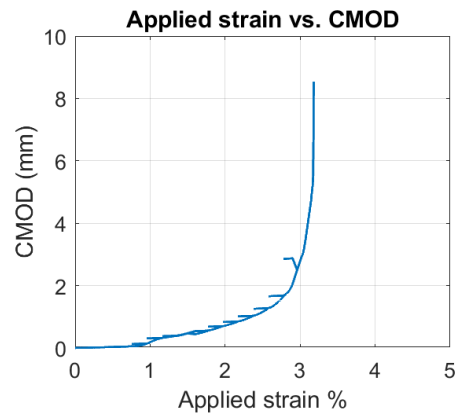
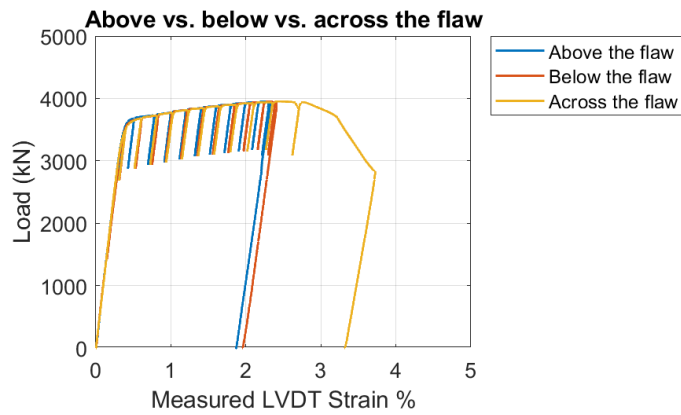
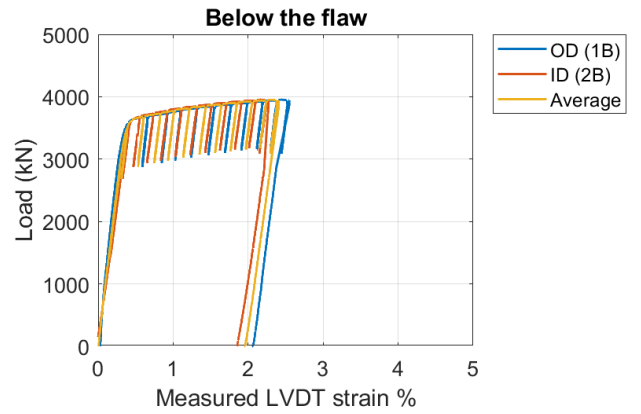
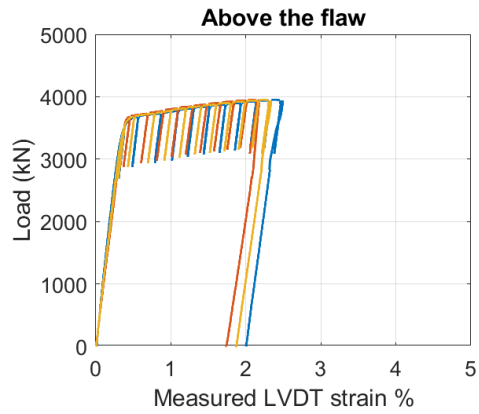
## CWP-13 WELD -40°C



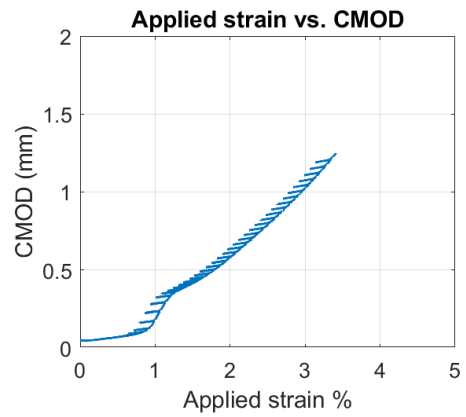
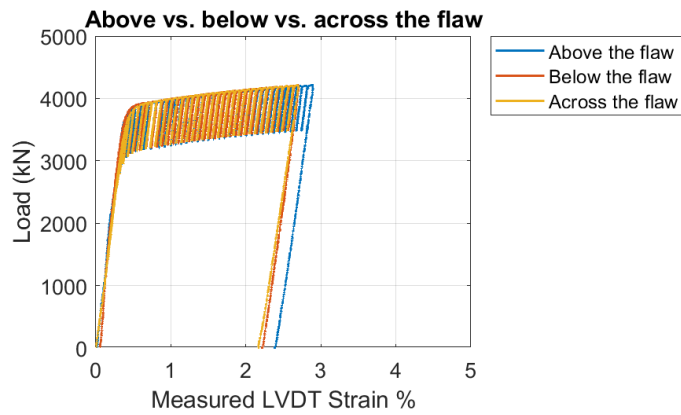
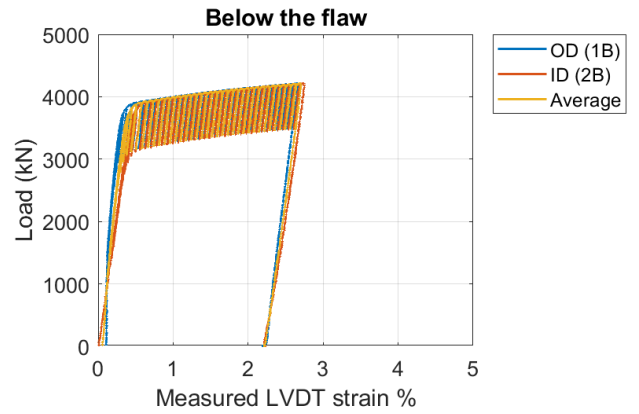
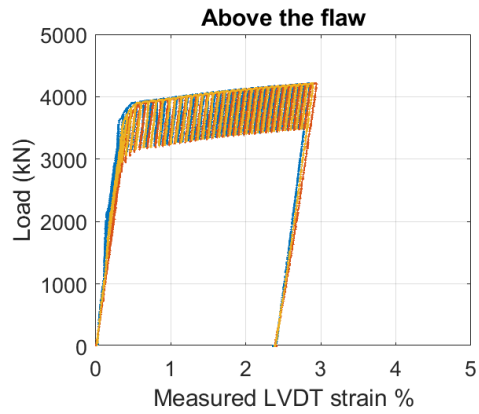
CWP-14 WELD -40°C



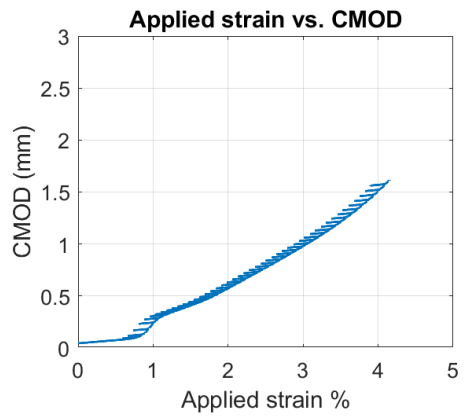
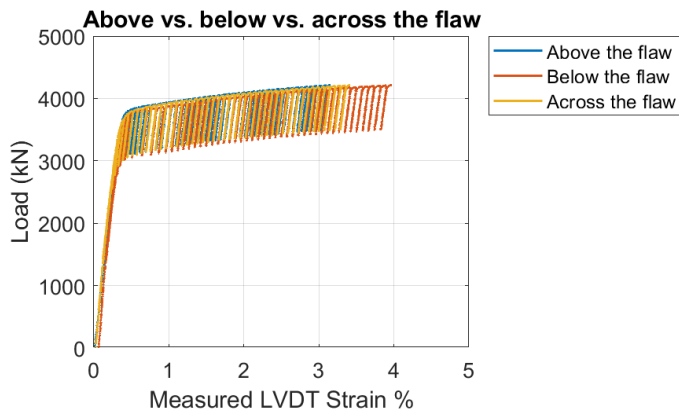
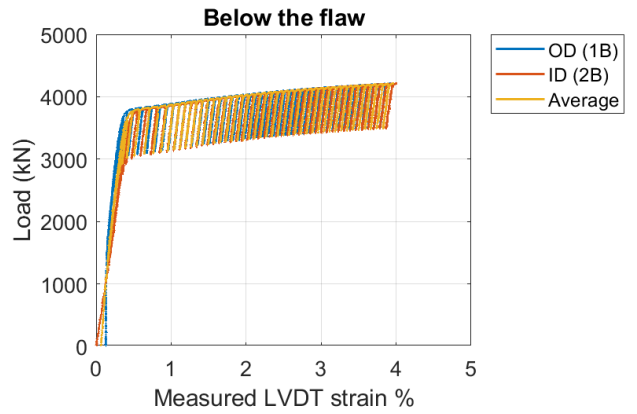
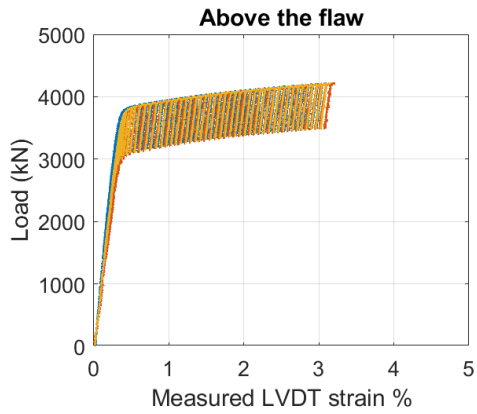
CWP-16 WELD 25°C



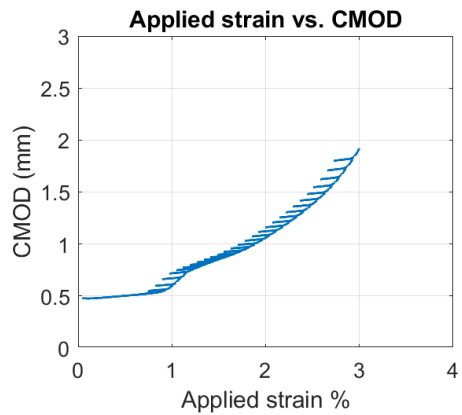
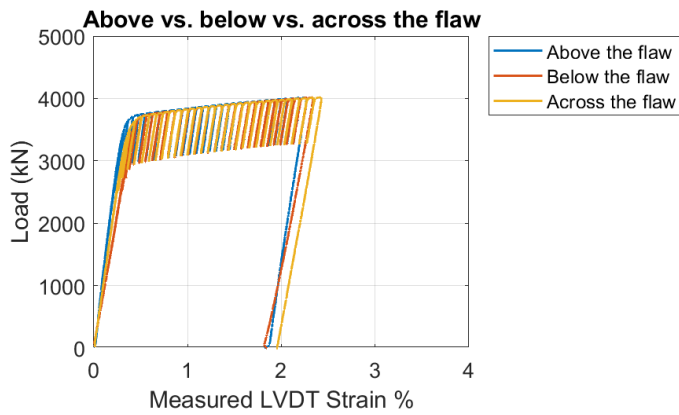
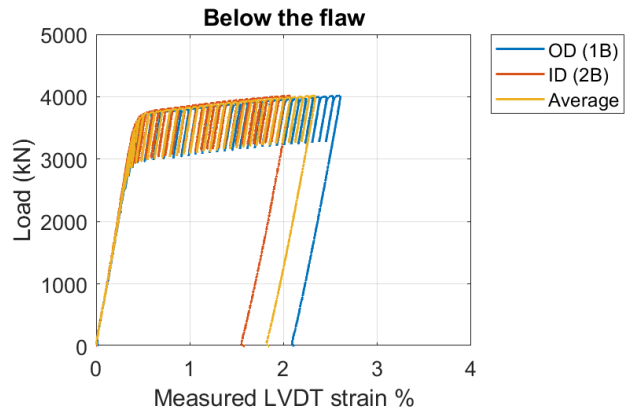
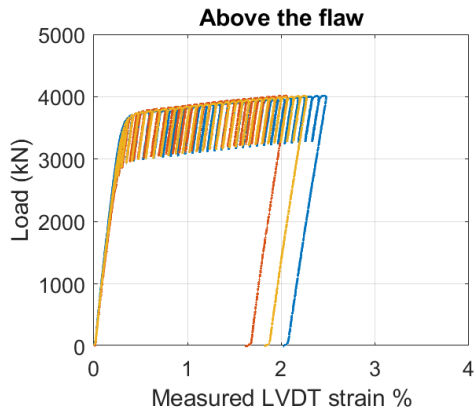
CWP-17 HAZ -40°C



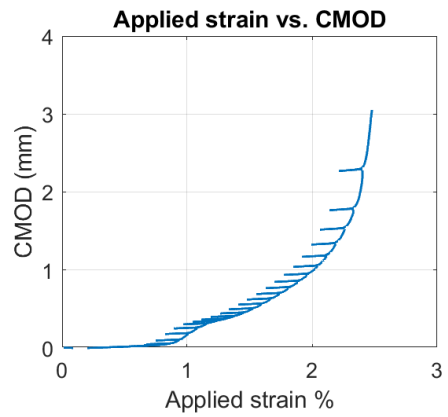
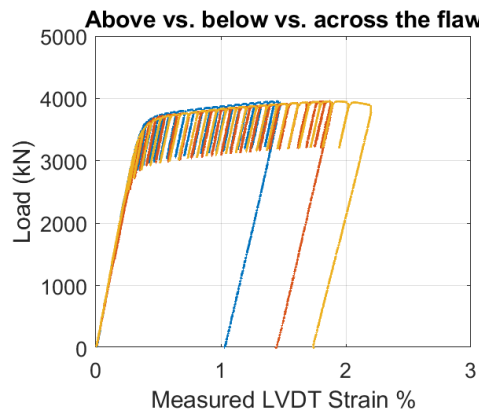
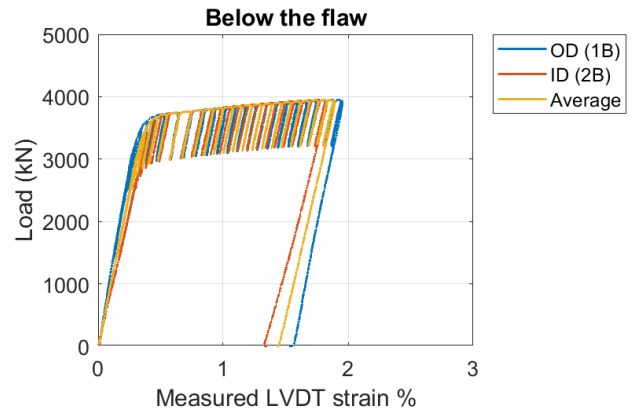
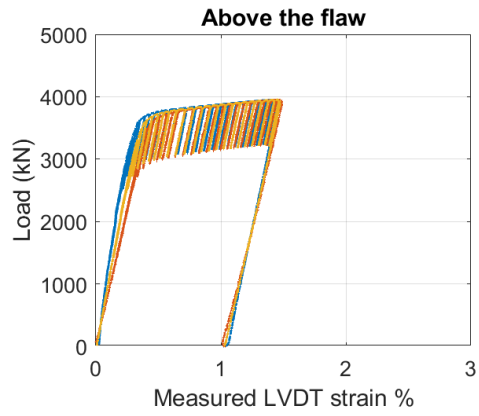
CWP-18 HAZ -40°C



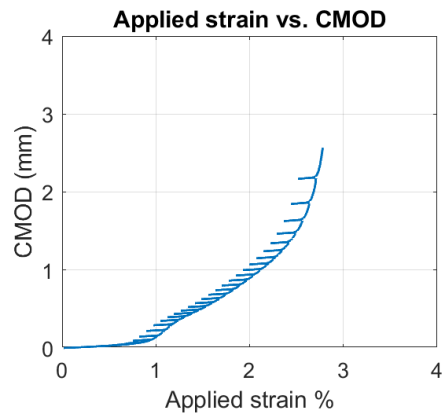
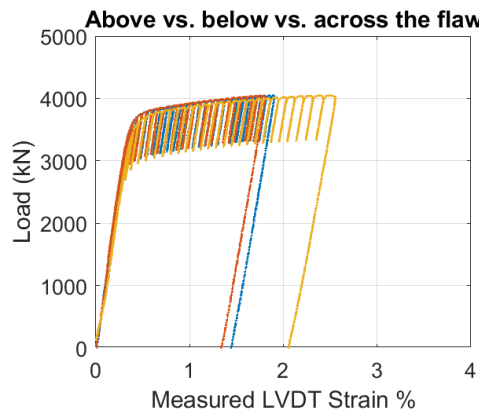
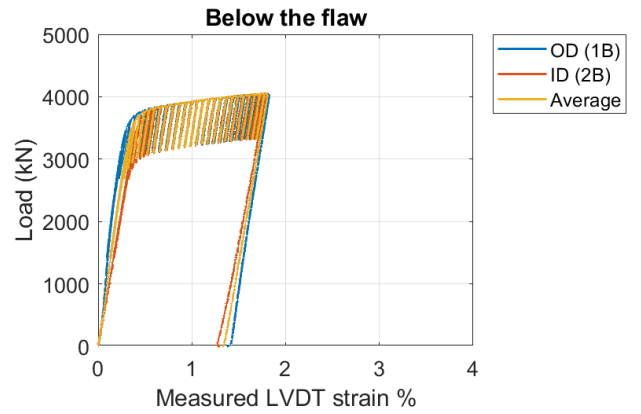
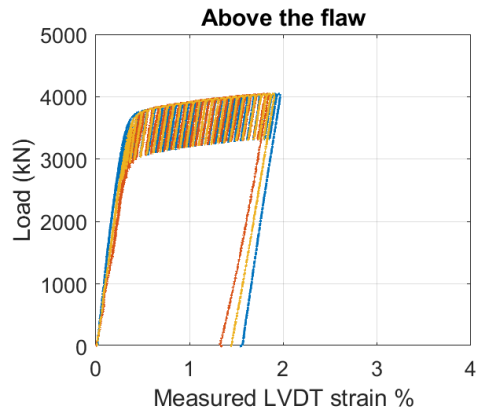
CWP-19 Weld -20°C



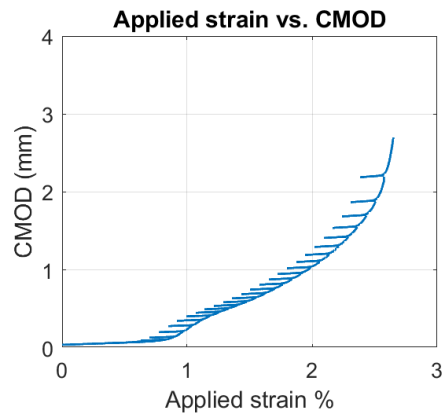
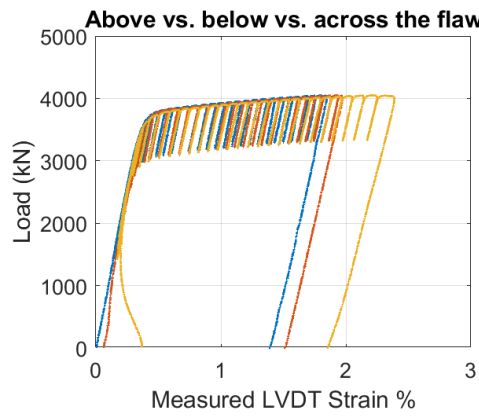
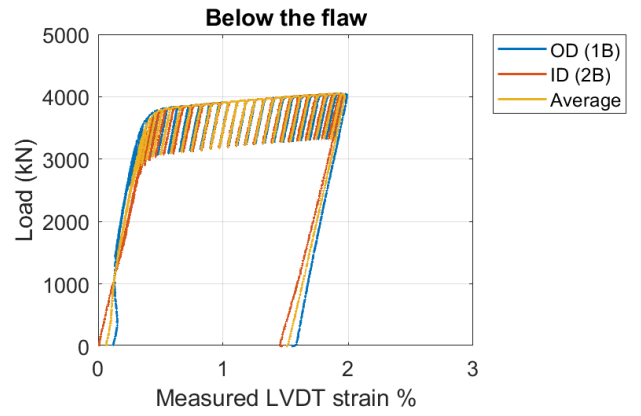
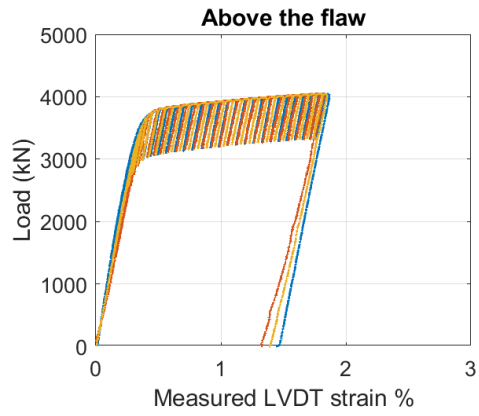
CWP-20 WELD 25°C



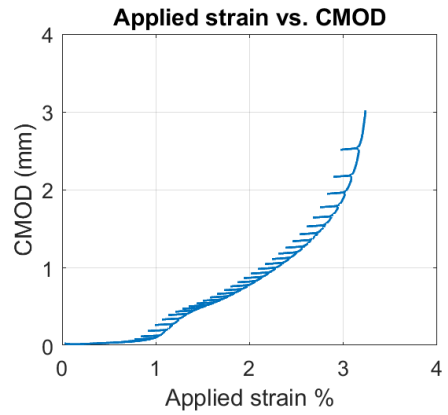
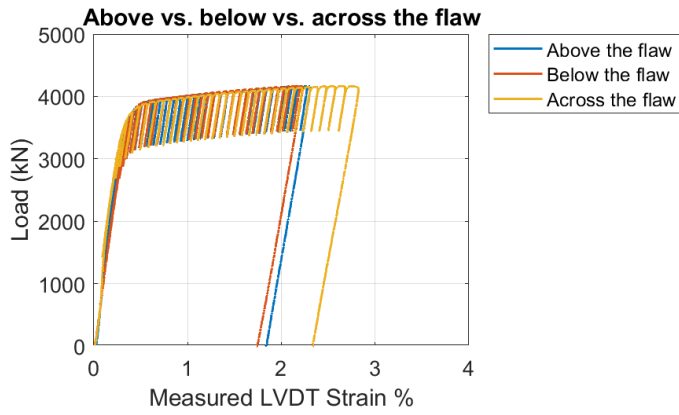
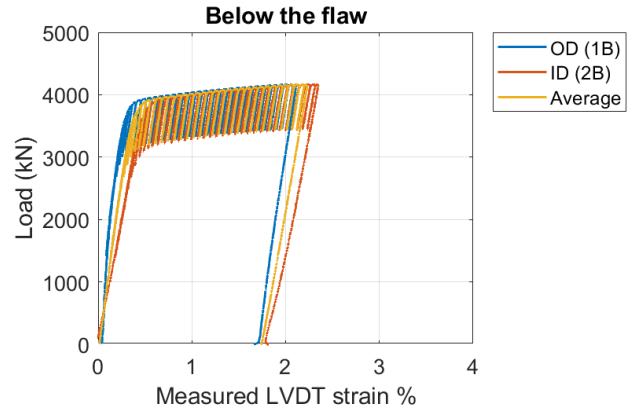
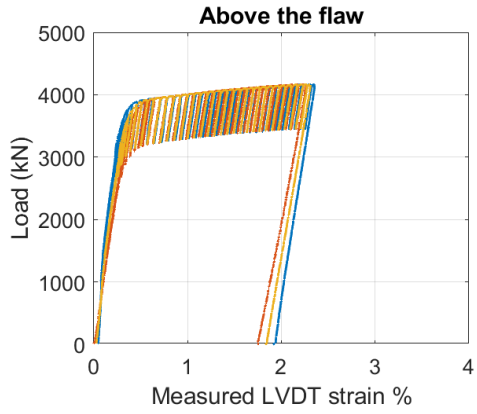
CWP-21 HAZ 25°C



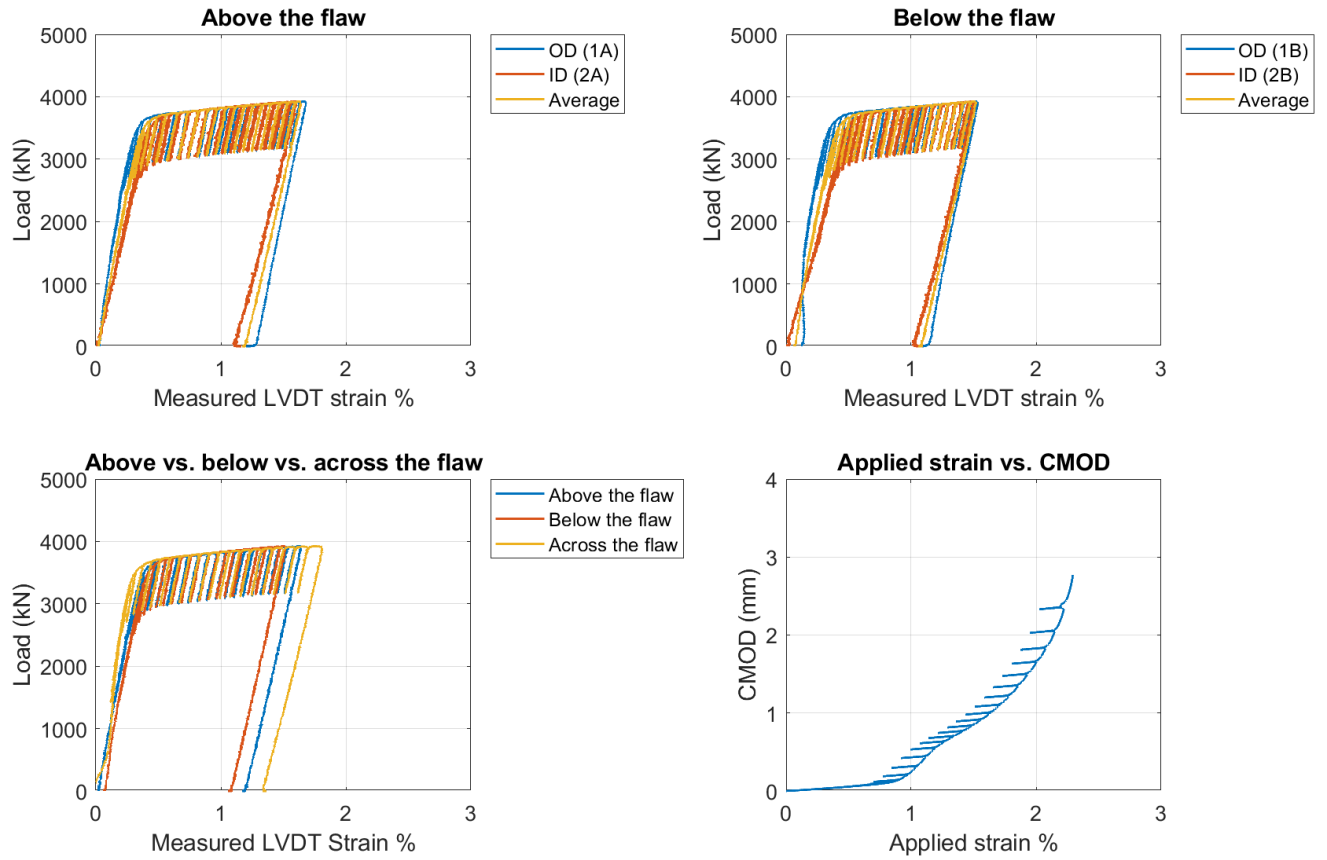
CWP-22 WELD -20°C



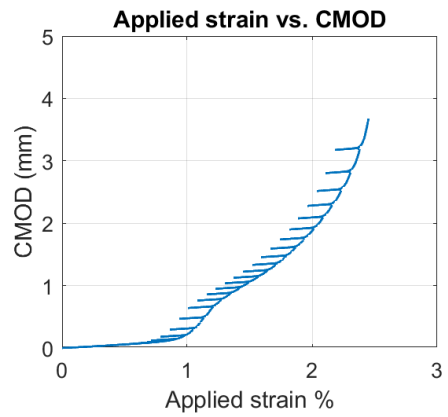
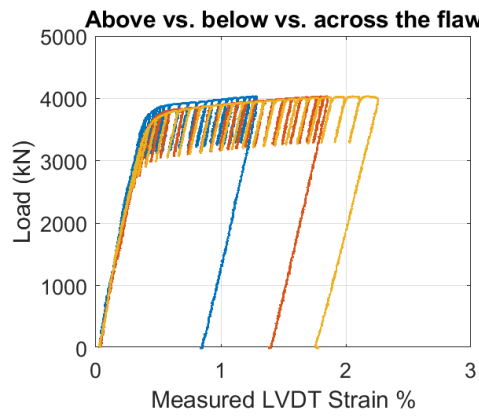
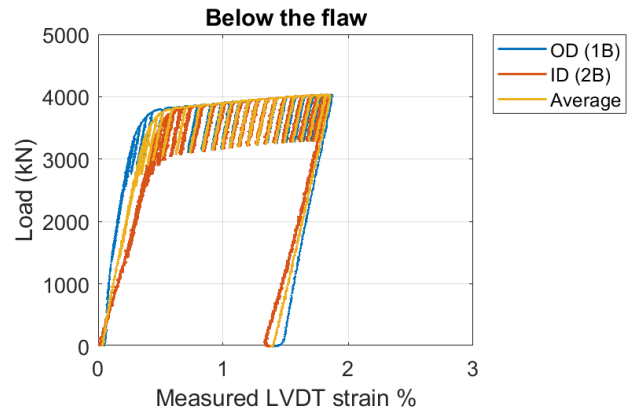
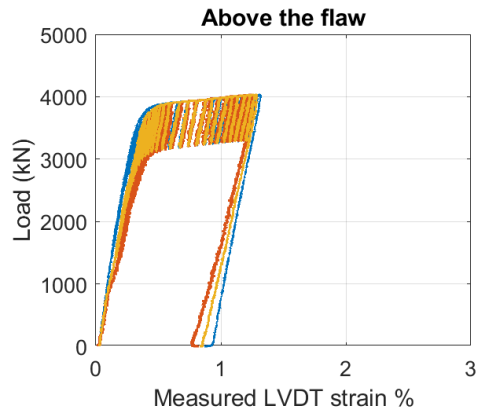
CWP-23 HAZ -20°C



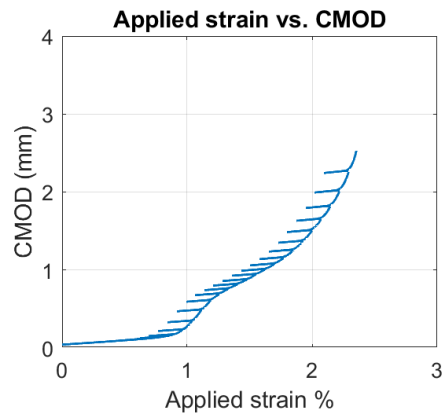
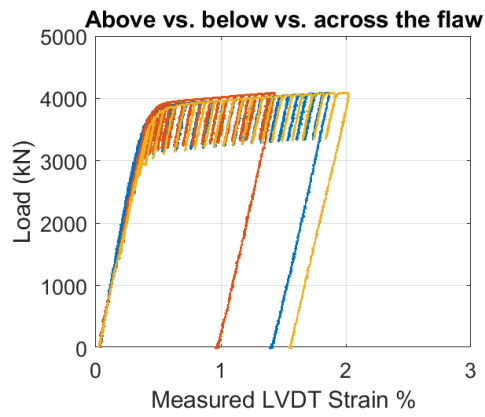
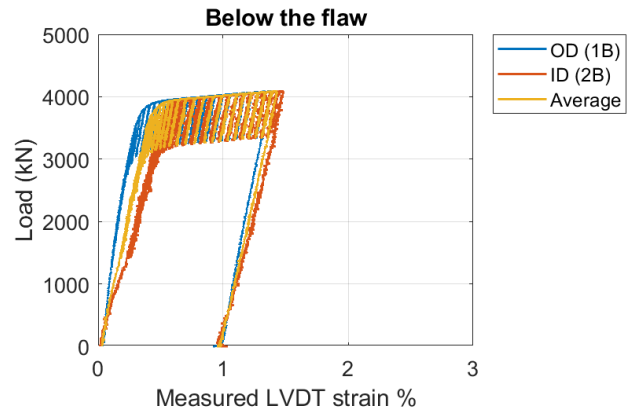
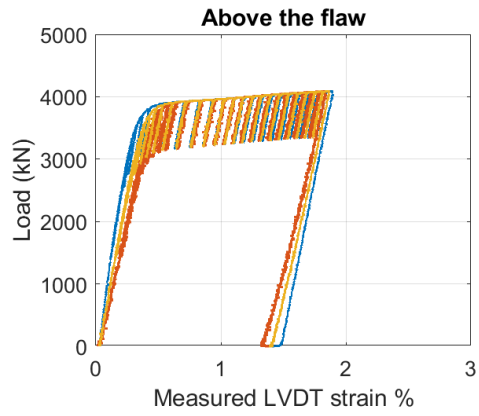
## CWP-24 Weld 25°C



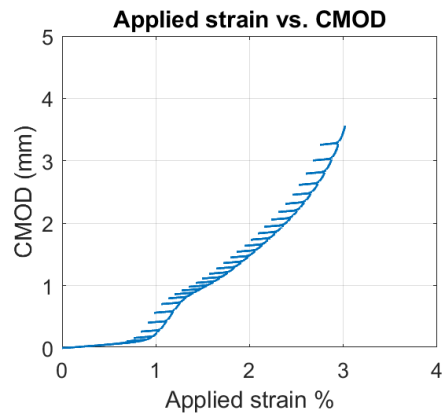
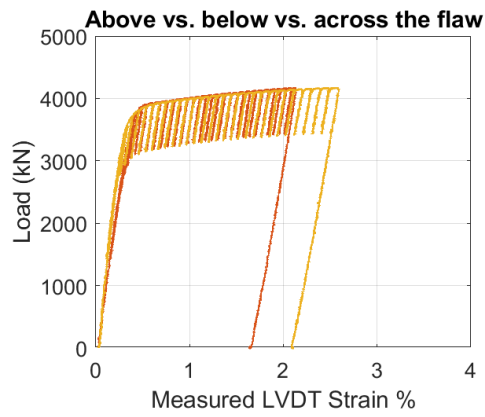
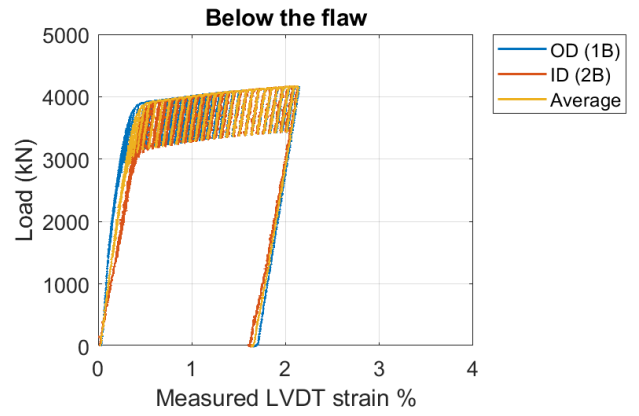
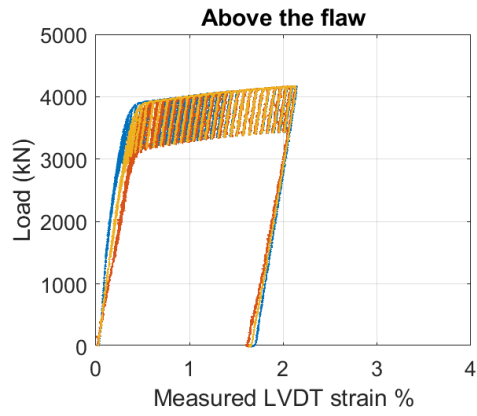
CWP-25 HAZ 25°C



CWP-26 Weld -20°C



CWP-27 HAZ -20°C



CWP-28 WELD -40°C

